# The Generation of Internal Tides over Steep Continental Slopes

P. G. Baines

*Phil. Trans. R. Soc. Lond. A* 1974 **277**, 27-58
doi: 10.1098/rsta.1974.0045

# THE GENERATION OF INTERNAL TIDES OVER STEEP CONTINENTAL SLOPES

By P. G. BAINES
*C.S.I.R.O. Division of Atmospheric Physics, Aspendale, Victoria* 3195, *Australia*

(*Communicated by C. H. B. Priestley, F.R.S. — Received* 2 *October* 1973)

## CONTENTS

A numerical procedure is presented for the calculation of internal tides generated by the interaction of surface tide with bottom topography which is tangent to the direction of internal tidal energy propagation at some depth. This procedure, together with that of Baines (1973), permits the calculation of internal tides generated by (virtually) arbitrary topography with horizontal scale greater than 1 km, and a wide range of realistic density stratifications.

The procedure is applied to continental slopes with simple linear and quarter-circle profiles, and constant stratification. For these cases, the largest internal tidal velocities and energy densities occur in regions around characteristics emanating from the tangential corner point; on the shallow shelf side the energy flux is a maximum in this region, but on the deep side it is a minimum and is distributed more evenly with depth. The total energy flux is greater than the maximum for flat-bump topography of comparable height by a factor of order 2–3. It increases nearly exponentially with height but is less sensitive to shape provided the slope is greater than critical, and is greater on the deep than on the shallow side by a factor of order 10. Calculations for more realistic density stratifications yield similar results.

The procedure is also applied to a real continental slope for which observations have been made by Wunsch & Hendry (1972), with stratification representing summer and winter conditions. The velocity fields and associated energy fluxes differ significantly from those of simple geometries, and are also sensitive to the seasonal density changes in the upper 50 m.

It is suggested that internal tidal generation will give rise to two mixing processes, one associated with the boundary layer near the tangent point and the other with shear instability in the velocity profile. Instability of the theoretical profiles according to the Richardson number criterion may be readily achieved in oceanic conditions.

The reflexion of an internal wave from a concave corner is discussed in an appendix, where it is shown that no singularities occur unless the radius of curvature is very large.

## 1. INTRODUCTION

Recent observations (Wunsch & Hendry 1972; Gould & McKee 1973) show that internal tides have large amplitudes over continental slopes. In the deep sea the observed amplitudes are somewhat smaller (see, for example, Fofonoff & Webster 1971), although internal tides of considerable amplitude have been observed over the mid-atlantic ridge (German North Atlantic Expedition 1938; see Defant 1961). These and other observations reinforce the notion that these waves are due to the interaction of the surface tide with bottom topography. An alternative resonance mechanism suggested by Krauss (1966) seems unlikely in view of the magnitude of dissipation (Le Blond 1966).

There have been three different approaches to the problem of generation by topography. Firstly, the topographic variations may be regarded as small perturbations on a horizontal bottom, so that the internal tide is driven by a linearized surface force. This method has been used by Cox & Sandstrom (1962), and applied by Munk (1966) and Bell (1973) to estimates of energy fluxes from random abyssal topography with given spectral distribution. Secondly, step-like topography has been treated by the method of horizontal matching of modes by Rattray, Dworsky & Kovala (1969) and Prinsenberg (1971). The third approach is to regard the internal tide as driven by a body force as described in Baines (1973). In the latter, a formalism is developed which is applicable to two-dimensional topography of arbitrary shape which is nowhere tangential to the local ray or characteristic for tidal frequency (i.e. ‘flat-bump’ topography). This theory is extended here to (almost) arbitrary topography and density stratifications. It is essentially two-dimensional in character but is applicable to three-dimensional topography where the radius of curvature is greater than the horizontal excursion of water particles in tidal motion, a distance of the order of 1 km.

The formulation of the generation problem for the simplest prototype case leads to what is believed to be a novel mathematical problem defined by equations (3.3)–(3.8). These equations are solved by a numerical iteration scheme described in §3, and the means by which it may be generalized to more complex topography and stratification are described in §4. With minor modifications the theory is also applicable to problems concerning the reflexion and transmission of internal waves encountering the same topography.

The wave fields generated at steep continental slopes with linear and quarter-circle profiles with constant stratification are discussed in detail in §§5 and 6, and compared with the corresponding results for ‘flat bump’ slopes. For linear slopes with slope $s$ and characteristic slope $c$, the wave field undergoes an abrupt change in amplitude as $s/c$ increases through unity, increasing on the deep right-hand side (hereafter denoted r.h.s. and similarly l.h.s. for the shallow left-hand side) but with essentially the same shape, and decreasing on the l.h.s., again with similar shape. The total generated energy flux increases by a factor of order 2–3, depending on topographic height. However, for $s/c$ greater than about 2 there is little change in the wave field and energy fluxes. As for the flat-bump situation there is a near exponential increase in the generated wave field with topographic height.

As expected from results of Baines (1971), a strong singularity in velocity develops on the tangential characteristic, whose strength increases with increasing topographic radius of curvature at the tangent point. Since this implies large vertical motions close to the boundary in this region it seems likely that this will give rise to significant mixing in the boundary layer. This mechanism, together with that associated with possible shear instability in the generated internal wave profile, is discussed in §7.

In §8 the foregoing theory is applied to a practical case, namely the north-west Atlantic continental slope in a region where measurements have been made by Wunsch & Hendry (1972), for two density stratifications representing summer and winter conditions. The generated velocity fields have more detail than those for the simpler topographies of §§5 and 6 because, over a considerable range of depths, $s/c$ has values near unity, rendering the wave field sensitive to smaller-scale topographic features in this region. It is also sensitive to density changes (seasonal and otherwise) in the top 50 m or so because the horizontal excursions of the rays or characteristics may be quite large here. The velocity measurements of Wunsch & Hendry are compared with the theoretical wave field but do not provide a good test of it. The total theoretical energy flux from the slope in the $M_2$ internal tide is of the order of 0.2 J s$^{-1}$ cm$^{-1}$ of slope length. Per unit area of the slope, this is comparable with the energy flux calculated by Bell (1973) from a mid ocean region of abyssal hills with a r.m.s. height of 109 m. The reason for this similarity is that the energy fluxes depend on the square of the barotropic tidal velocity, which is typically 5 cm/s for the latter and 0.44 cm/s for the former, normal to the slope. This indicates that although the continental slopes are probably the most effective and coherent generators of internal tides in the ocean, their relative importance compared with abyssal topography is reduced because the normal barotropic velocities are frequently small due to the presence of the adjacent coastline.

## 2. Basic equations and formulation of the generation problem

A summary only of the relevant equations is given below, since the equations and notation for the internal wave motion and the barotropic tide are the same as in Baines (1973), to which the reader is referred for more details. Taking the equations governing the internal tides to be those of a rotating stratified inviscid fluid and assuming that they are linear for tidal phenomena yields

$$\left.\begin{aligned} \rho_0\frac{\partial \boldsymbol{u}}{\partial t}+\rho_0\boldsymbol{f}\times\boldsymbol{u}+\nabla p+\rho g\hat{\boldsymbol{z}} &= 0,\\ \frac{\partial \rho}{\partial t}+w\frac{\mathrm{d}\rho_0}{\mathrm{d}z} = 0, \quad \nabla\cdot\boldsymbol{u} &= 0, \end{aligned}\right\} \tag{2.1}$$

where $\boldsymbol{u}$ is the fluid velocity, $\boldsymbol{f}$ the Coriolis parameter, $p_0$, $\rho_0$ the pressure and density in static equilibrium, $p$, $\rho$ the perturbations from this state due to the wave motion, $g$ the acceleration due to gravity, $t$ the time variable and $\hat{\boldsymbol{z}}$ the unit vector in the upward vertical direction. We next write $\boldsymbol{u} = \boldsymbol{u}_1+\boldsymbol{u}_\mathrm{i}$, $p = p_1+p_\mathrm{i}$ where $\boldsymbol{u}_1$, $p_1$ denote the flow field for a corresponding unstratified ocean of density $\overline{\rho_0}$, the mean of $\rho_0$, which has the same surface displacement as the one being considered. In order to determine the internal tide $\boldsymbol{u}_{\mathrm{i}}$ one must first observe or calculate the barotropic tide $\boldsymbol{u}_1$ which satisfies

$$\left.\begin{aligned} \frac{\partial \boldsymbol{u}_1}{\partial t} + \boldsymbol{f}\times\boldsymbol{u}_1 + \frac{1}{\rho_0}\nabla p_1 + g\hat{\boldsymbol{z}} &= \boldsymbol{F}, \\ \nabla\cdot\boldsymbol{u}_1 &= 0, \end{aligned}\right\} \tag{2.2}$$

with boundary conditions

$$\left.\begin{aligned} \boldsymbol{u}_1\cdot\nabla(z+h(x)) &= 0, \quad \text{on} \quad z = -h(x), \\ (\mathrm{D}/\mathrm{D}t)\,(z-\eta(x,t)) &= 0, \quad \text{on} \quad z = \eta(x,t), \end{aligned}\right\} \tag{2.3}$$

where $\boldsymbol{F}$ is the tide-generating force, $\eta$ the tide surface height, $x$ and $z$ horizontal and vertical coordinates respectively and $z = -h(x)$ is the equation of the ocean bottom. For semi-diurnal tides over continental slopes it may readily be shown from considerations of scale that, to a good approximation, $u_1$ is a function of $x$ and $t$ only and

$$\partial(hu_1)/\partial x = 0, \tag{2.4}$$

so that we may write

$$hu_1 = Q\cos\omega t, \tag{2.5}$$

where the volume flux $Q$ is a constant and $\omega$ is the tidal frequency. Considerations of continuity then yield that

$$w(x,z,t) = -Qz(1/h)_x\cos\omega t, \tag{2.6}$$

where the suffix denotes a derivative. In many practical cases of continental slopes we will have

$$Q \simeq a_0\omega d,$$

where $d$ is the width of the continental shelf and $a_0$ is the amplitude of the surface tide at the coastline. Subtracting equations (2.2) (in linearized form) from equations (2.1) yields

$$\begin{gathered} \frac{\partial \boldsymbol{u}_{\mathrm{i}}}{\partial t} + \boldsymbol{f}\times\boldsymbol{u}_{\mathrm{i}} + \frac{1}{\rho_0}\nabla p_{\mathrm{i}} + \frac{\rho g\hat{\boldsymbol{z}}}{\rho_0} = 0, \\ \nabla\cdot\boldsymbol{u}_{\mathrm{i}} = 0, \quad \frac{\partial\rho}{\partial t} + w_{\mathrm{i}}\frac{\mathrm{d}\rho_0}{\mathrm{d}z} - w_1\frac{\mathrm{d}\rho_0}{\mathrm{d}z} = 0. \end{gathered} \tag{2.7}$$

Defining the stream function $\psi$ by

$$u_{\mathrm{i}} = -\psi_z, \quad w_{\mathrm{i}} = \psi_x, \tag{2.8}$$

then gives

$$\nabla^2\psi_{tt} + N^2\psi_{xx} + f^2\psi_{zz} = -N^2(z)\,w_{1x}, \tag{2.9}$$

where

$$N^2 = -\frac{g}{\rho_0}\frac{\mathrm{d}\rho_0}{\mathrm{d}z},$$

with the boundary conditions

$$\left.\begin{aligned} \psi &= 0 \quad \text{on} \quad z = 0, \\ \psi &= 0, \quad \text{on} \quad z = -h(x). \end{aligned}\right\} \tag{2.10}$$

The origin is taken at the free surface, the latter being regarded as stationary as far as the internal wave dynamics are concerned. From equations (2.6) and (2.9) we obtain the field equation

$$\nabla^2\psi_{tt} + N^2\psi_{xx} + f^2\psi_{zz} = QN^2(z)\,z(1/h)_{xx}\cos\omega t, \tag{2.11}$$

for the internal tidal motion. For solutions at the tidal forcing frequency only we may write

$$\psi = \Psi(x,z)\,\mathrm{e}^{-\mathrm{i}\omega t}, \tag{2.12}$$

which yields

$$\Psi_{xx} - c^2(z)\,\Psi_{zz} = \frac{Q}{1-\omega^2/N^2}z\left(\frac{1}{h}\right)_{xx}, \quad c^2 = \frac{\omega^2-f^2}{N^2-\omega^2}. \tag{2.13}$$

In order to solve this equation we first obtain a particular solution $\Psi_2$, which has the form

$$\Psi_2 = \frac{Q}{1-\omega^2/N^2}\frac{z}{h(x)}. \tag{2.14}$$

This is exact for constant $N^2$ and a good approximation for oceanic situations at tidal frequencies. We then write

$$\Psi = \Psi_2 + \Psi_3, \tag{2.15}$$

and want to solve the homogeneous form of (2.13) for $\Psi_3$ such that the boundary conditions (2.10) and the appropriate radiation conditions on the internal waves are satisfied, namely

$$\Psi_3 = 0 \quad \text{on} \quad z = 0,$$

$$\Psi_3 = Q\left(1 + \frac{c^2}{1-f^2/\omega^2}\right) \quad \text{on} \quad z = -h(x). \tag{2.16}$$

If $c(z)$ has the form

$$c = c_0\,(1+c_1 z)^2, \tag{2.17}$$

where $c_0, c_1$ are constants, the general solution for $\Psi_3$ is

$$\Psi_3 = c(z)^{\frac{1}{2}}\,(f(\xi) + g(\eta)), \tag{2.18}$$

where $f$, $g$ are arbitrary functions of the characteristic variables

$$\xi = \int_0^z \frac{\mathrm{d}z}{c} + x, \quad \eta = \int_0^z \frac{\mathrm{d}z}{c} - x.$$

Henceforth it will be assumed that the density stratification has this form. Arbitrary density distributions may be approximated by piecewise sections satisfying (2.17), as discussed in §4. Modes in a channel of depth $h_{\mathrm{L}}$ have the form

$$\psi_n = c_0^{\frac{1}{2}}(1+c_1 z)\sin\frac{n\pi z(1-c_1 h_{\mathrm{L}})}{h_{\mathrm{L}}(1+c_1 z)}\exp\left[\mathrm{i}(n\pi c_0(1-c_1 h_{\mathrm{L}})\,x/h_{\mathrm{L}} - \omega t)\right], \tag{2.19}$$

where $n$ is an integer.† Group velocities for these modes may be defined by

$$c_{\mathrm{g}} = \text{mean energy flux/mean energy density},$$

yielding

$$c_{\mathrm{g}} = \frac{\omega n\pi h_{\mathrm{L}}(1-f^2/\omega^2)}{c_0[(1+\beta c_0^2)\,n^2\pi^2(1-c_1 h_{\mathrm{L}}) + (1+f^2/\omega^2)^{\frac{1}{4}}\,c_1^2 h_{\mathrm{L}}^2]}, \tag{2.20}$$

where

$$\beta = \tfrac{1}{5}(1 + (1-c_1 h_{\mathrm{L}}) + (1-c_1 h_{\mathrm{L}})^2 + (1-c_1 h_{\mathrm{L}})^3 + (1-c_1 h_{\mathrm{L}})^4). \tag{2.21}$$

To proceed further we need to specify the geometry of the system under consideration, and we first discuss the formalism for the simplest case for steep topography, which is represented in figure 1. The topography is of arbitrary shape except that (*a*) there are only two points on the bottom surface where a characteristic is tangential to the surface namely $\mathrm{P_a}$ and $\mathrm{P_b}$, and (*b*) choosing the coordinate origin at the point where the tangential characteristic at $\mathrm{P_a}$ meets the surface, the topography outside the range spanned by the characteristics $\xi = 0$ and $\eta = 0$ is assumed to be horizontal. We take the depth on the deep side to be $h_{\mathrm{R}}$ and the depth on the shallow side to be $h_{\mathrm{L}}$, and define

$$\gamma_{\mathrm{L}} = \int_{-h_{\mathrm{L}}}^{0}\frac{\mathrm{d}z}{c} = \frac{h_{\mathrm{L}}}{c_0(1-c_1 h_{\mathrm{L}})}, \quad A_{\mathrm{L}} = \frac{Q}{c(-h_{\mathrm{L}})^{\frac{1}{2}}\,(1-\omega^2/N^2(-h_{\mathrm{L}}))} \tag{2.22}$$

---

† Equations (4.25), (4.46), (4.51) and (6.5) of Baines (1973) contain errors and should read as the corresponding equations in this paper, namely (2.19), (2.35), (2.37) and (5.3).

and similarly for $\gamma_R$, $A_R$. It may then be readily shown (see Baines 1973) that on the left-hand side (l.h.s.)

$$f(\xi) = -\frac{A_L \xi}{2\gamma_L} + f_p(\xi) \quad (\xi < 0), \tag{2.23}$$

where $f_p(\xi)$ is periodic with period $2\gamma_L$ and must satisfy the radiation condition

$$f_p(\xi) = \frac{i}{2\gamma_L} P \int_{-2\gamma_L}^{0} f_p(s) \cot \frac{\pi}{2\gamma_L}(s-\xi)\, ds \quad (-2\gamma_L < \xi < 0), \tag{2.24}$$

where $P$ denotes the Cauchy principal value, and similarly on the r.h.s.

$$g(\eta) = \frac{-A_R \eta}{2\gamma_R} + g_p(\eta) \quad (\eta < 0), \tag{2.25}$$

where $g_p(\eta)$ has period $2\gamma_R$ and

$$g_p(\eta) = \frac{i}{2\gamma_R} P \int_{-2\gamma_R}^{0} g_p(s) \cot \frac{\pi}{2\gamma_R}(s-\eta)\, ds \quad (-2\gamma_R < \eta < 0). \tag{2.26}$$

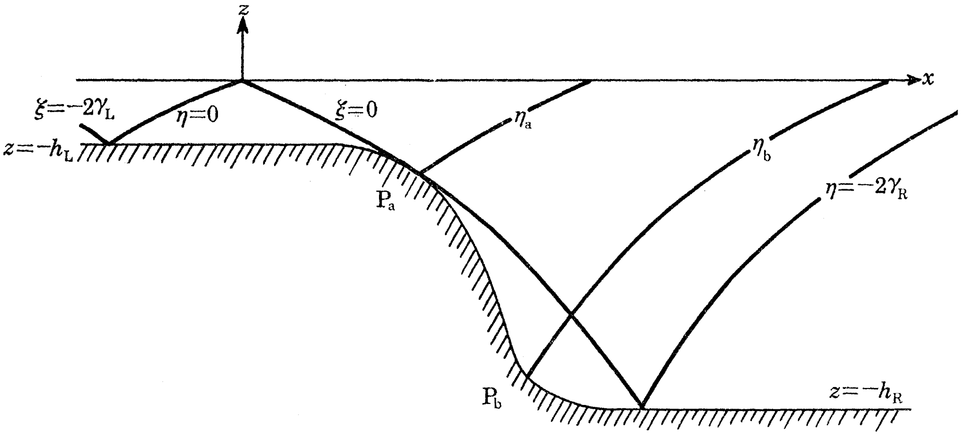

FIGURE 1. The geometry for the simplest case of a steep continental slope, showing the rays or characteristics for the internal tidal motion.

The boundary conditions (2.10) in terms of $f$ and $g$ are

$$\left.\begin{aligned} f(\xi)+g(\eta) &= 0 \quad \text{on} \quad z = 0,\\ f(\xi)+g(\eta) &= \frac{Q}{c(z)^{\frac{1}{2}}}\left(1+\frac{c^2(z)}{1-f^2/\omega^2}\right) = A(\eta) \quad \text{on} \quad z = -h(x). \end{aligned}\right\} \tag{2.27}$$

The bottom surface may be written

$$\left.\begin{aligned} &\xi = -K_2(\eta) \quad \text{or} \quad \eta = -H_2(\xi), \quad -2\gamma_R < \eta < \eta_a,\\ \text{and} \quad &\xi = -K_1(\eta) \quad \text{or} \quad \eta = -H_1(\xi), \quad \eta_a < \eta < 0, \end{aligned}\right\} \tag{2.28}$$

where all these functions are single-valued, and $\eta_a$ is the $\eta$-characteristic at $P_a$. Further, for each characteristic $\eta$ in the range $-2\gamma_R < \eta < \eta_a$ there is a corresponding characteristic $\phi(\eta)$ in the same range such that

$$K_2(\phi(\eta)) = K_2(\eta). \tag{2.29}$$

The characteristics $\eta$ and $\phi(\eta)$ intersect the bottom surface on the same $\xi$-characteristic. Clearly, if $\eta_b$ is the $\eta$-characteristic at $P_b$ we have

$$\phi(\eta_b) = \eta_b, \tag{2.30}$$

and also, in general,

$$\phi(\phi(\eta)) = \eta, \tag{2.31}$$

and

$$\phi(\eta_a) = -2\gamma_R. \tag{2.32}$$

We regard the function $\phi(\eta)$ as being defined by equation (2.29). The second of equations (2.27) then yields that

$$\left.\begin{aligned} f(\xi)+g(\eta) &= A(\eta), \quad \text{on} \quad \xi = -K_1(\eta), \quad -2\gamma_L < \xi < 0, \\ &\qquad\qquad\qquad\qquad\qquad\qquad \eta_a < \eta < 0, \\ g(\eta)-g(\phi(\eta)) &= A(\eta)-A(\phi(\eta)), \quad \text{for} \quad -2\gamma_R < \eta < \eta_a, \end{aligned}\right\} \tag{2.33}$$

with $\phi(\eta)$ as defined by equation (2.29). Equations (2.33) together with equations (2.23)–(2.26) constitute the problem to be solved for the functions $f(\xi)$ and $g(\eta)$, and it is assumed that there is a unique solution.

The internal wave velocity field is given by

$$\boldsymbol{u}_i = \boldsymbol{u}_2+\boldsymbol{u}_3, \tag{2.34}$$

where $\boldsymbol{u}_2$ is given by the stream function $\Psi_2$ and

$$\left.\begin{aligned} u_3 &= \frac{Q}{h_L}-\frac{1}{c_0^{\frac{1}{2}}(1+c_1 z)}\,(f_p'(\xi)+g_p'(\eta))-c_0^{\frac{1}{2}}c_1(f_p(\xi)+g_p(\eta)), \\ w_3 &= c_0^{\frac{1}{2}}(1+c_1 z)\,(f_p'(\xi)-g_p'(\eta)), \end{aligned}\right\} \tag{2.35}$$

on the l.h.s. of the topography, with

$$\text{energy flux} = \overline{\rho_0}\frac{(\omega^2-f^2)}{\omega}\int_{-2\gamma_L}^{0} f_{pr}(\xi)f_{pi}'(\xi)\,\mathrm{d}\xi, \tag{2.36}$$

where suffixes r and i denote real and imaginary parts, and

$$\begin{aligned} \text{energy density} = {} & \tfrac{1}{2}\overline{\rho_0}\left(1+\int_{-h_L}^{0} c(z)^2\,\mathrm{d}z/h_L\right)\int_{-2\gamma_L}^{0}(f_{pr}'(\xi)^2+f_{pi}'(\xi)^2)\,\mathrm{d}\xi \\ & +(1+f^2/\omega^2)\frac{c_0 c_1^2 h_L\overline{\rho_0}}{8\gamma_L}\int_{-2\gamma_L}^{0}(f_{pr}(\xi)^2+f_{pi}(\xi)^2)\,\mathrm{d}\xi. \end{aligned} \tag{2.37}$$

Similar expressions may be written down for the r.h.s. From these relations and equation (2.20) an 'effective mode number' $n_e$ may be defined. This gives an estimate of the dominant modes present without requiring Fourier decomposition.

## 3. The iteration procedure

The above equations (2.23–2.26, 2.33) were solved numerically by means of a double iteration procedure. Various other (simpler) iterative schemes and manipulations of the system were investigated, but the only one which converged to the correct answer was that given below.

In order to standardize the system we make the following change of variables

$$\left.\begin{aligned} \theta = \frac{\eta}{\gamma_R}, \quad \theta_a = \frac{\eta_a}{\gamma_R}, \quad M(\theta) = \frac{K(\eta)}{\gamma_L}, \quad G(\theta) = g(\eta), \\ \bar{A}(\theta) = A(\eta), \quad \Phi(\theta) = \phi(\eta). \end{aligned}\right\} \tag{3.1}$$

We then write
$$\left.\begin{aligned} G(\theta) &= \bar{A}(\theta)+G_{\mathrm{p}}(\theta) \quad (-2<\theta<\theta_{\mathrm{a}}),\\ G(\theta) &= \bar{A}(\theta)-\tfrac{1}{2}A_{\mathrm{L}}M(\theta)+G_{\mathrm{p}}(\theta) \quad (\theta_{\mathrm{a}}<\theta<0),\end{aligned}\right\} \tag{3.2}$$

where, from equations (2.23), (2.25) we see that

$$G_{\mathrm{p}}(-2) = G_{\mathrm{p}}(\theta_{\mathrm{a}}) = G_{\mathrm{p}}(0). \tag{3.3}$$

$G_{\mathrm{p}}(\theta)$ must then satisfy the following set of equations:

$$G_{\mathrm{p}}(\theta) = -\tfrac{1}{2}\mathrm{i}P\int_{\theta_{\mathrm{a}}}^{0} G_{\mathrm{p}}(s)\cot\tfrac{1}{2}\pi\,(M(s)-M(\theta))\,M'(s)\,\mathrm{d}s \quad (\theta_{\mathrm{a}}<\theta<0), \tag{3.4}$$

$$G_{\mathrm{p}}(\Phi(\theta)) = G_{\mathrm{p}}(\theta) \quad (-2<\theta<\theta_{\mathrm{a}}), \tag{3.5}$$

where $\Phi(\theta)$ is defined by
$$M(\Phi(\theta)) = M(\theta) \quad (-2<\theta<\theta_{\mathrm{a}}), \tag{3.6}$$

and
$$\mathrm{D}(\theta) = \tfrac{1}{2}\mathrm{i}P\int_{-2}^{0} \mathrm{D}(s)\cot\tfrac{1}{2}\pi\,(s-\theta)\,\mathrm{d}s \quad (-2<\theta<0), \tag{3.7}$$

where
$$\left.\begin{aligned} \mathrm{D}(\theta) &= \tfrac{1}{2}A_{\mathrm{R}}\theta-A_{\mathrm{L}}M(\theta)+\bar{A}(\theta)+G_{\mathrm{p}}(\theta) \quad (\theta_{\mathrm{a}}<\theta<0),\\ &= \tfrac{1}{2}A_{\mathrm{R}}\theta+\bar{A}(\theta)+G_{\mathrm{p}}(\theta) \quad (-2<\theta<\theta_{\mathrm{a}}).\end{aligned}\right\} \tag{3.8}$$

These equations (3.3–3.8) present a novel mathematical problem to be solved for the function $G_{\mathrm{p}}(\theta)$. The method of solution is first of all to ignore the integral condition (3.4) and iterate to find a function satisfying all the remaining equations. From this function $(G_{\mathrm{p}}^{\mathrm{I}}(\theta))$ one may obtain another function $(\bar{G}_{\mathrm{p}}^{\mathrm{II}}(\theta))$ which satisfies (3.4) but violates equation (3.7). This violation $(\bar{G}_{\mathrm{p}}^{\mathrm{II}}(\theta)-G_{\mathrm{p}}^{\mathrm{I}}(\theta))$ may then be used as a starting-point for a second cycle of iterations omitting equation (3.4) (the inner loop). The process of satisfying (3.4) while violating (3.7) is then repeated (the outer loop), and so on. The procedure is complicated by the need to consider combinations of successive iterates in order to ensure convergence, in each of the inner and outer loops. In the symbols used below, the superscript refers to the outer loop while the two subscripts refer to the inner loop.

To start the iteration procedure we first define

$$\begin{aligned} R_{11}^{\mathrm{I}}(\theta) &= A_{\mathrm{R}}\tfrac{1}{2}\theta-A_{\mathrm{L}}\tfrac{1}{2}M(\theta)+\bar{A}(\theta) \quad (\theta_{\mathrm{a}}<\theta<0),\\ &= \tfrac{1}{2}\bar{A}_{\mathrm{R}}\theta+\bar{A}(\theta) \quad (-2<\theta<\theta_{\mathrm{a}}),\end{aligned} \tag{3.9}$$

and
$$R_{12}^{\mathrm{I}}(\theta) = \tfrac{1}{2}\mathrm{i}P\int_{-2}^{0} R_{11}^{\mathrm{I}}(s)\cot\tfrac{1}{2}\pi\,(s-\theta)\,\mathrm{d}s. \tag{3.10}$$

We next obtain a new function $R_{13}^{\mathrm{I}}(\theta)$ from $R_{12}^{\mathrm{I}}(\theta)$ which satisfies the boundary condition (3.5) and also (3.3). The simplest way of doing this is to take

$$\left.\begin{aligned} R_{13}^{\mathrm{I}}(\theta) &= \tfrac{1}{2}(R_{12}^{\mathrm{I}}(\Phi(\theta))+R_{12}^{\mathrm{I}}(\theta)) \quad (-2<\theta<\theta_{\mathrm{a}}),\\ &= R_{12}^{\mathrm{I}}(\theta)+R_{12}^{\mathrm{I}}(\theta_{\mathrm{a}})-R_{12}^{\mathrm{I}}(0)\\ &\quad -(\theta/\theta_{\mathrm{a}})\,(R_{12}^{\mathrm{I}}(\theta_{\mathrm{a}})-R_{12}^{\mathrm{I}}(0)) \quad (\theta_{\mathrm{a}}<\theta<0).\end{aligned}\right\} \tag{3.11}$$

We also define
$$R_{14}^{\mathrm{I}}(\theta) = R_{13}^{\mathrm{I}}(\theta)-R_{12}^{\mathrm{I}}(\theta). \tag{3.12}$$

Ignoring the l.h.s. radiation condition (equation (3.4)) the result of this first iteration in the inner loop is

$$G_{\mathrm{p}_1}^{\mathrm{I}}(\theta) = R_{13}^{\mathrm{I}}(\theta), \tag{3.13}$$

PHILOSOPHICAL TRANSACTIONS OF THE ROYAL SOCIETY A MATHEMATICAL, PHYSICAL & ENGINEERING SCIENCES

which satisfies the boundary condition exactly and fails to satisfy the r.h.s. radiation condition with the error $R^{\mathrm{I}}_{14}(\theta)$. For the second cycle we therefore take

$$R^{\mathrm{I}}_{21}(\theta) = R^{\mathrm{I}}_{14}(\theta), \tag{3.14}$$

and repeat the procedure to equation (3.12). Numerical investigation shows that, if subsequent iterations are taken in this manner, the functions $R^{\mathrm{I}}_{i+13}(\theta)$, $R^{\mathrm{I}}_{i+23}(\theta)$, etc., alternate in sign. To increase the rate of convergence of the iteration, at every cycle except the first the expression

$$\int_{-2}^{0} |p_i R^{\mathrm{I}}_{i4}(\theta) + (1-p_i)\, R^{\mathrm{I}}_{i-14}(\theta)|^2 \, \mathrm{d}\theta$$

was minimized numerically as a function of $p_1$. The required value of $p_1$ is given by

$$p_i = (T_2 - T_3)/(T_1 + T_2 - 2T_3),$$

where
$$T_1 = \int_{-2}^{0} R^{\mathrm{I}}_{i4}(\theta)\, R^{\mathrm{I}}_{i4}(\theta)^* \,\mathrm{d}\theta, \quad T_2 = \int_{-2}^{0} R^{\mathrm{I}}_{i-14}(\theta)\, R^{\mathrm{I}}_{i-14}(\theta)^* \,\mathrm{d}\theta,$$

$$T_3 = \frac{1}{2}\int_{-2}^{0} (R^{\mathrm{I}}_{i4}(\theta)\, R^{\mathrm{I}}_{i-14}(\theta)^* + R^{\mathrm{I}}_{i4}(\theta)^*\, R^{\mathrm{I}}_{i-14}(\theta))\,\mathrm{d}\theta, \tag{3.15}$$

the asterisk denoting complex conjugate. For the second iteration we have $i = 2$, and for the first, $p_1 = 1$. The result of the second iteration in this loop is then

$$G^{\mathrm{I}}_{\mathrm{p}2}(\theta) = G^{\mathrm{I}}_{\mathrm{p}1}(\theta) + p_2 R^{\mathrm{I}}_{23}(\theta) \tag{3.16}$$

satisfying the conditions (3.3), (3.5), exactly and equation (3.7) with the error

$$R^{\mathrm{I}}_{31}(\theta) = p_2 R^{\mathrm{I}}_{24}(\theta) + (1-p_2)\, R^{\mathrm{I}}_{14}(\theta). \tag{3.17}$$

This cycle is then repeated as often as is necessary until the desired accuracy is obtained, yielding a function $G^{\mathrm{I}}_{\mathrm{p}}(\theta)$ which satisfies both the boundary conditions (3.3), (3.5) and the r.h.s. radiation condition (3.7). For the $i$th iteration we have

$$\left.\begin{aligned}
R^{\mathrm{I}}_{i1}(\theta) &= p_{i-1} R^{\mathrm{I}}_{i-14}(\theta) + (1-p_{i-1})\, R^{\mathrm{I}}_{i-24}(\theta),\\
R^{\mathrm{I}}_{i2}(\theta) &= \tfrac{1}{2}\mathrm{i}P\int_{-2}^{0} R^{\mathrm{I}}_{i1}(s)\cot\tfrac{1}{2}\pi\,(s-\theta)\,\mathrm{d}s,\\
R^{\mathrm{I}}_{i3}(\theta) &= \tfrac{1}{2}(R^{\mathrm{I}}_{i2}(\Phi(\theta)) + R^{\mathrm{I}}_{i2}(\theta)) \quad (-2 < \theta < \theta_{\mathrm{a}}),\\
&= R^{\mathrm{I}}_{i2}(\theta) + R^{\mathrm{I}}_{i\ 3}(\theta_{\mathrm{a}}) - R^{\mathrm{I}}_{i2}(0) - (\theta/\theta_{\mathrm{a}})\,(R^{\mathrm{I}}_{i2}(\theta_{\mathrm{a}}) - R^{\mathrm{I}}_{i2}(0)) \quad (\theta_{\mathrm{a}} < \theta < 0),\\
R^{\mathrm{I}}_{i4}(\theta) &= R^{\mathrm{I}}_{i3}(\theta) - R^{\mathrm{I}}_{i2}(\theta),
\end{aligned}\right\} \tag{3.18}$$

yielding
$$G^{\mathrm{I}}_{\mathrm{p}i}(\theta) = G^{\mathrm{I}}_{\mathrm{p}i-1}(\theta) + p_i R^{\mathrm{I}}_{i3}(\theta), \tag{3.19}$$

with the error term, the starting-point for the next iteration,

$$R^{\mathrm{I}}_{i+11}(\theta) = p_i R^{\mathrm{I}}_{i4}(\theta) + (1-p_i)\, R^{\mathrm{I}}_{i-14}(\theta). \tag{3.20}$$

The rate of convergence depends markedly on the value of $\theta_{\mathrm{a}}$. With 40 grid points in each range $-2 < \theta < \theta_{\mathrm{a}}$ and $\theta_{\mathrm{a}} < \theta < 0$, for $|1+\theta_{\mathrm{a}}|$ less than about 0.4 convergence is fairly rapid, accuracy to within 1 % being obtained after about four iterations. However, as $\theta_{\mathrm{a}}$ decreases the number of iterations required increases, and ten may be required for 2 % accuracy when $\theta_{\mathrm{a}} = -0.2$. The rate of convergence depends less strongly on the slope of the topography.

The function $G_{\mathrm{p}}^{\mathrm{I}}(\theta)$ will not, in general, satisfy the l.h.s. radiation condition, equation (3.4). We therefore define the function

$$\begin{aligned} S^{\mathrm{I}}(\theta) &= -\tfrac{1}{2}\mathrm{i}P\int_{\theta_{\mathrm{a}}}^{0} G_{\mathrm{p}}^{\mathrm{I}}(s)\cot\tfrac{1}{2}\pi\left(M(s)-M(\theta)\right)M'(s)\,\mathrm{d}s \quad &&(\theta_{\mathrm{a}}<\theta<0),\\ &= 0, &&(-2<\theta<\theta_{\mathrm{a}}), \end{aligned} \tag{3.26}$$

and also,
$$\bar{G}_{\mathrm{p}}^{\mathrm{II}}(\theta) = G_{\mathrm{p}}^{\mathrm{I}}(\theta)+S^{\mathrm{I}}(\theta), \quad R_{11}^{\mathrm{II}}(\theta) = S^{\mathrm{I}}(\theta). \tag{3.27}$$

$\bar{G}_{\mathrm{p}}^{\mathrm{II}}(\theta)$ will then satisfy the l.h.s. radiation condition but not that on the r.h.s. $R_{11}^{\mathrm{II}}(\theta)$ is then taken as the starting-point for a second series of iterations on the r.h.s. (inner) loop as defined by equations (3.9)–(3.20), resulting in the function $G_{\mathrm{p}}^{\mathrm{II}}(\theta)$. $S^{\mathrm{II}}(\theta)$ is then defined in the same way as for $S^{\mathrm{I}}(\theta)$. It transpires that, if the double loop iteration scheme is continued in this manner, the successive functions $\bar{G}_{\mathrm{p}}^{J}(\theta)$, $\bar{G}_{\mathrm{p}}^{J+1}(\theta)$ oscillate in sign about the desired limiting value, sometimes with increasing amplitude, and do not converge. However, we may again make use of the oscillatory character to determine a procedure which will converge, as follows.

Suppose we take

$$\left.\begin{aligned} \bar{G}_{\mathrm{p}}^{J}(\theta) &= \bar{G}_{\mathrm{p}}^{J-1}(\theta)+G_{\mathrm{p}}^{J-1}(\theta)+S^{J-1}(\theta),\\ \bar{G}_{\mathrm{p}}^{J+1}(\theta) &= \bar{G}_{\mathrm{p}}^{J}(\theta)+G_{\mathrm{p}}^{J}(\theta)+S^{J}(\theta)\\ &= \bar{G}_{\mathrm{p}}^{J-1}(\theta)+G_{\mathrm{p}}^{J-1}(\theta)+S^{J-1}(\theta)+G_{\mathrm{p}}^{J}(\theta)+S^{J}(\theta). \end{aligned}\right\} \tag{3.28}$$

Then a combination of these two,

$$q_J\bar{G}_{\mathrm{p}}^{J+1}(\theta)+(1-q_J)\,\bar{G}_{\mathrm{p}}^{J}(\theta)$$

will also satisfy the l.h.s. radiation condition and the boundary condition, and have the error term

$$q_J S^{J}(\theta)+(1-q_J)\,S^{J-1}(\theta)$$

with respect to the r.h.s. radiation condition (i.e. this part of the function does not satisfy the condition). The aim, therefore, is to choose $q_J$ such that this error term is minimized, and minimizing

$$\int_{\theta_{\mathrm{a}}}^{0}|q_J S^{J}(\theta)+(1-q_J)\,S^{J-1}(\theta)|^2\,\mathrm{d}\theta,$$

yields, as for equations (3.15), (3.16),

$$q_J = (T_5-T_6)/(T_4+T_5-2T_6), \tag{3.29}$$

where
$$\left.\begin{aligned} T_4 &= \int_{\theta_{\mathrm{a}}}^{0} S^{J}(\theta)\,S^{J}(\theta)^*\,\mathrm{d}\theta, \quad T_5 = \int_{\theta_{\mathrm{a}}}^{0} S^{J-1}(\theta)\,S^{J-1}(\theta)^*\,\mathrm{d}\theta,\\ T_6 &= \frac{1}{2}\int_{\theta_{\mathrm{a}}}^{0}\left(S^{J}(\theta)\,S^{J-1}(\theta)^*+S^{J}(\theta)^*\,S^{J-1}(\theta)\right)\mathrm{d}\theta. \end{aligned}\right\} \tag{3.30}$$

Hence, for the second iteration in the outer loop we take

$$\bar{G}_{\mathrm{p}}^{\mathrm{III}}(\theta) = \bar{G}_{\mathrm{p}}^{\mathrm{II}}(\theta)+q_{\mathrm{II}}\left(G_{\mathrm{p}}^{\mathrm{II}}(\theta)+S^{\mathrm{II}}(\theta)\right), \tag{3.31}$$

with
$$R_{11}^{\mathrm{III}}(\theta) = q_{\mathrm{II}}S^{\mathrm{II}}(\theta)+(1-q_{\mathrm{II}})\,S^{\mathrm{I}}(\theta). \tag{3.32}$$

In every case calculated $q_J$ was a number between 0 and 1. All subsequent iterations in this second, outer loop are carried out in the same manner as the second iteration, until the desired accuracy is obtained, $\bar{G}^{J}_{\mathrm{p}}(\theta)$ representing the $J$th approximation to $G_{\mathrm{p}}(\theta)$. The number of iterations required is again rather insensitive to the topographic slope but strongly dependent on the ratio of the depths $h_{\mathrm{L}}/h_{\mathrm{R}}$, or more accurately, on the value of $\theta_{\mathrm{a}}$. For values of $|\theta_{\mathrm{a}}| \leqslant 0.2$ the rate of convergence is very slow†, 10 or more iterations being required for tolerable accuracy (say 2–3 %), whereas for $|\theta_{\mathrm{a}}| \approx 1$ this accuracy is obtained within 6 iterations.

To summarize the complete iteration scheme to find the function $G_{\mathrm{p}}(\theta)$, $-2 < \theta < 0$, satisfying equations (3.3)–(3.8), we first construct the functions $R^{\mathrm{I}}_{11}(\theta)$, $R^{\mathrm{I}}_{12}(\theta)$, $R^{\mathrm{I}}_{13}(\theta)$, $R^{\mathrm{I}}_{14}(\theta)$ from equations (3.9)–(3.13), obtaining $G^{\mathrm{I}}_{\mathrm{p}1}(\theta)$, $R^{\mathrm{I}}_{21}(\theta)$ from (3.13), (3.14). We then continue iterating in this inner loop via equations (3.18)–(3.20), where $p_i$ is defined by equations (3.15), until the error term $R^{\mathrm{I}}_{i+11}(\theta)$ is sufficiently small. If this occurs after the $j$th iteration, we take $G^{\mathrm{I}}_{\mathrm{p}}(\theta) = G^{\mathrm{I}}_{\mathrm{p}j}(\theta)$, and then we define $S^{\mathrm{I}}(\theta)$ via equation (3.26) and $\bar{G}^{\mathrm{II}}_{\mathrm{p}}(\theta)$, $R^{\mathrm{II}}_{11}(\theta)$ by equation (3.27). We then return to the inner loop and obtain $R^{\mathrm{II}}_{12}(\theta)$, $R^{\mathrm{II}}_{13}(\theta)$, $R^{\mathrm{II}}_{14}(\theta)$, etc., from equations (3.10)–(3.14), and then make successive iterations from equations (3.18)–(3.20) until convergence is obtained yielding $G^{\mathrm{II}}_{\mathrm{p}}(\theta)$. The quantity $S^{\mathrm{II}}(\theta)$ is then obtained from equations (3.26) and $\bar{G}^{\mathrm{III}}_{\mathrm{p}}(\theta)$, $R^{\mathrm{III}}_{11}(\theta)$ from equations (3.31), (3.32) where $q_{\mathrm{II}}$ is obtained from (3.29), (3.30). $R^{\mathrm{III}}_{11}(\theta)$ is then used to begin the third inner loop, and equations (3.31), (3.32) are used in all subsequent iterations in the outer loop.

Having obtained $G_{\mathrm{p}}(\theta)$ and hence $G(\theta)$, the corresponding stream function on the l.h.s. in dimensionless form may be defined as

$$F(\zeta) = f(\zeta), \quad \zeta = \xi/\gamma_{\mathrm{L}}, \tag{3.33}$$

and from equations (2.33), (3.1), given by

$$F(\zeta) = \bar{A}(\theta) - G(\theta). \tag{3.34}$$

The function $F_{\mathrm{p}}(\zeta)$ representing the internal wave motion is then given by

$$F_{\mathrm{p}}(\zeta) = F(\zeta) + \tfrac{1}{2}A_{\mathrm{L}}\zeta. \tag{3.35}$$

The derivatives $G'_{\mathrm{p}}(\theta)$, $F'_{\mathrm{p}}(\zeta)$ represent vertical velocity profiles, and the results of subsequent sections are presented in terms of these functions. We then have

$$\left.\begin{aligned} f'_{\mathrm{p}}(\xi) &= QF'_{\mathrm{p}}(\zeta)/\gamma_{\mathrm{L}} \quad \text{on the l.h.s.} \\ g'_{\mathrm{p}}(\eta) &= QG'_{\mathrm{p}}(\theta)/\gamma_{\mathrm{R}} \quad \text{on the r.h.s.,} \end{aligned}\right\} \tag{3.36}$$

and the actual fluid velocities and energy fluxes and densities may be computed from equations (2.35)–(2.37). For $\theta_{\mathrm{a}} = -0.2$ the total computing time required is about 8 min on a CDC 3600.

## 4. Procedures for more complex topography and stratification, and incident waves

The procedure developed in the preceding two sections for a simple continental slope may readily be extended to a variety of other situations, so that virtually all conceivable two-dimensional situations of practical interest are soluble by these methods. Some such situations are illustrated in figure 2. Not all of these have been treated but the author is confident that satisfactory convergence may be obtained within computing time which is comparable (possibly larger by a factor of 2 or 3 for cases (*b*), (*c*) and (*d*)) to that for the simplest case.

† For $|\theta_{\mathrm{a}}|$ very small ($< 0.05$) the system appeared not to be converging at all. However, it is believed that convergence may be achieved by increasing the number of grid points.

The procedures for solving the generation problem for the various geometries represented in figure 2 are as follows. For case (*a*) the radiation conditions on the l.h.s. and r.h.s. imposed where the bottom is horizontal may be transformed by reflexion of the characteristics from the top and bottom to apply to the range of characteristics along the line AA′, in the manner indicated in Baines (1973). The problem will then be of the same type as that described in § 3, with the form of the intervening topography being represented in the radiation conditions. After solving the problem by the iteration procedure the total velocity field may be constructed by successive reflexions away from AA′. Case (*b*) is similar to the § 3 problem except that the l.h.s. radiation condition now applies to the r.h.s. characteristics emanating from region FC and DE of the bottom.

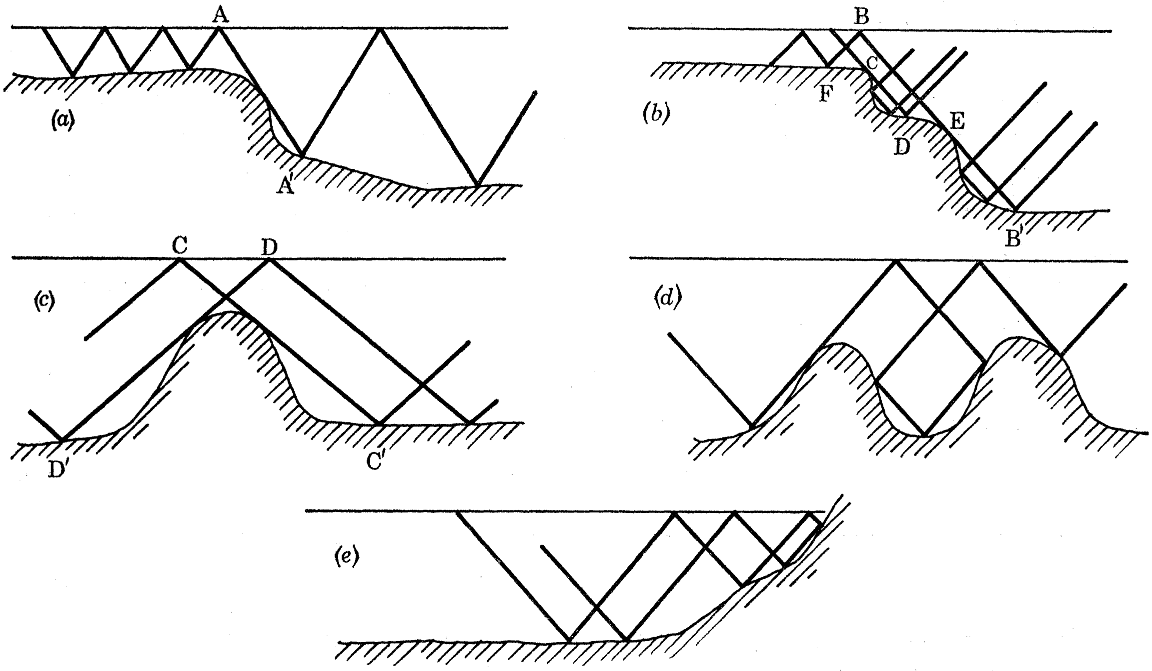

FIGURE 2. Examples of topography to which the procedures developed in the text may be applied. Straight characteristics have been drawn for simplicity.

The r.h.s. iteration loop may be carried out in the same manner, except that we now have two separate regions – CD and EB′ – where boundary conditions of the form (3.5) must be satisfied. For case (*c*) one first satisfies (say) the r.h.s. conditions by iteration on the range CC′, as before but then must also iterate on the l.h.s. on the range DD′ in the same manner in order to satisfy both the boundary and radiation conditions there. One then returns to the r.h.s. and repeats the process. More complex situations such as case (*d*) may be treated in the same manner, provided that such characteristics emerge from the topography after a finite number of reflexions (i.e. there are no closed loops or limit cycles). Situations as complex as this are likely to be very laborious in practice, as such characteristics must be traced through the system and the functional relations determined. Case (*e*) is a degenerate form of the same class of problem, equations (3.4)–(3.8) with $\theta_a = 0$, and only the single one-sided iterative loop is required.

The characteristic procedure for all kinds of topography shown in figure 2 may also be applied to situations where equation (2.17) is satisfied in layers. From the boundary conditions of continuity of pressure and displacement at an internal interface (see for example, Yih 1965), it may readily be seen (from linear theory) that there is no reflexion from the interface if $\rho_0(z)$ and $N(z)$

are both continuous there. Hence the above theory may be used with a wider range of characteristic curves constructed from piecewise sections each satisfying (2.17) for various $c_0$, $c_1$, provided $\rho_0(z)$ and $N(z)$ are continuous at the interfaces. In particular, stratification containing a thermocline (or several thermoclines) may be modelled in this way (figure 3). In fact one may so model almost any continuous density stratification and clearly the fewer the number of junctions required the better will be the approximation. However, the procedure will break down if there is significant internal reflexion of wave energy from layers or abrupt changes in density.

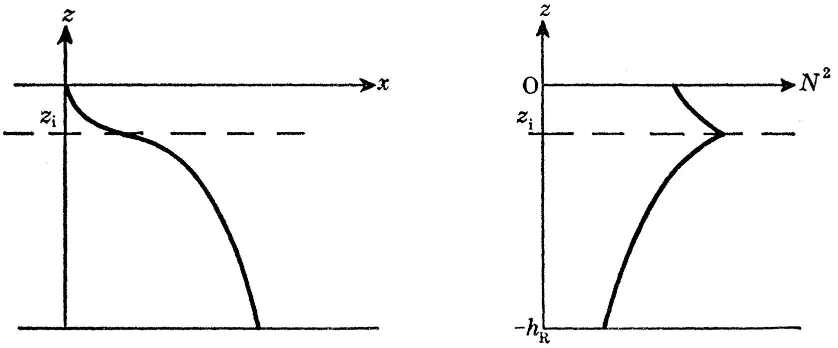

FIGURE 3. A typical characteristic and corresponding $N^2$ profile for a two-layer model of a thermocline. $\rho_0(z)$ and $N(z)$ must be continuous at $z_i$.

The methods described in this paper may also be applied to the reflexion–diffraction problem of internal waves incident on the same class of topography. The procedures will be the same, except that the initial functions used to start the iteration must be suitably modified. A suitable initial wave field for this type of problem is that obtained by the continuation of the incident wave on characteristics by reflexion from the boundaries.

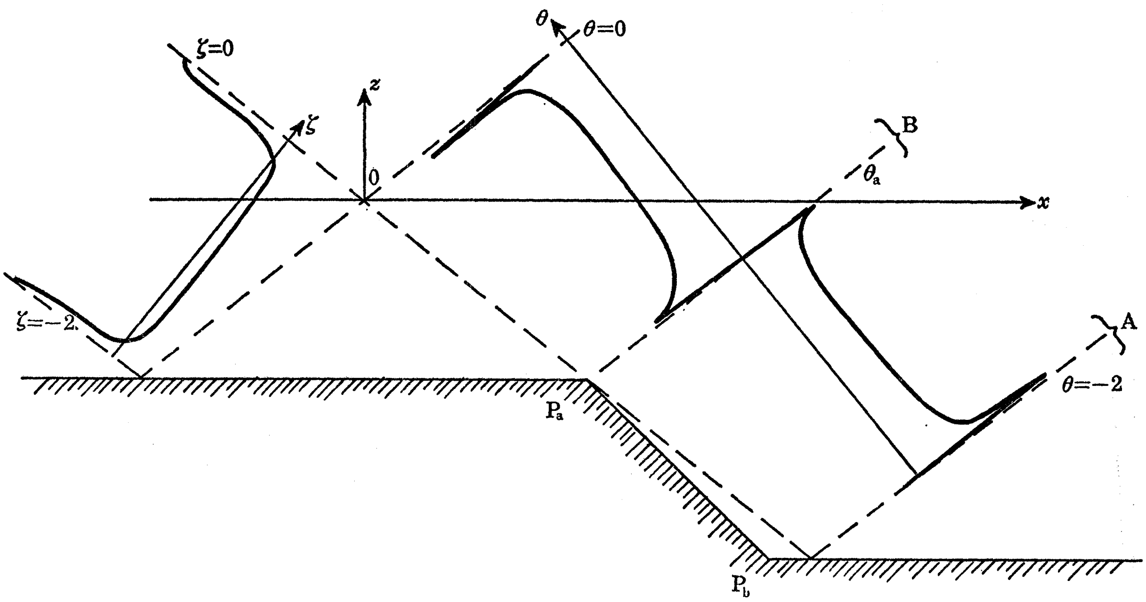

FIGURE 4. Topography for a linear slope with $h_L/h_R = 0.5$. Ranges for the velocity profile functions of figure 5 are indicated, the profiles drawn (not to scale) representing the baroclinic motion when the barotropic velocity is at its maximum from right to left. Regions A and B, each comprising $\frac{1}{16}$ of the characteristic range (5 grid points) are indicated.

## 5. Steep linear slopes

We first apply the above procedure to the simplest case of a linear continental slope in an ocean with constant $N$, as in § 6 of Baines (1973), so that the results of these two sections together describe the internal waves generated by all such simple slopes under these conditions. Choosing the coordinate origin at the point where the characteristic which is tangent to the topography at the top-most corner meets the free surface gives, as the equation for the topography,

$$\left.\begin{aligned} z &= -h_{\mathrm{L}}, & -\infty < x < h_{\mathrm{L}}/c,\\ z &= -h_{\mathrm{L}} - s(x - h_{\mathrm{L}}/c), & h_{\mathrm{L}}/c < x < (h_{\mathrm{R}} - h_{\mathrm{L}})/s + h_{\mathrm{L}}/c,\\ z &= -h_{\mathrm{R}}, & x > (h_{\mathrm{R}} - h_{\mathrm{L}})/s + h_{\mathrm{L}}/c, \end{aligned}\right\} \qquad (5.1)$$

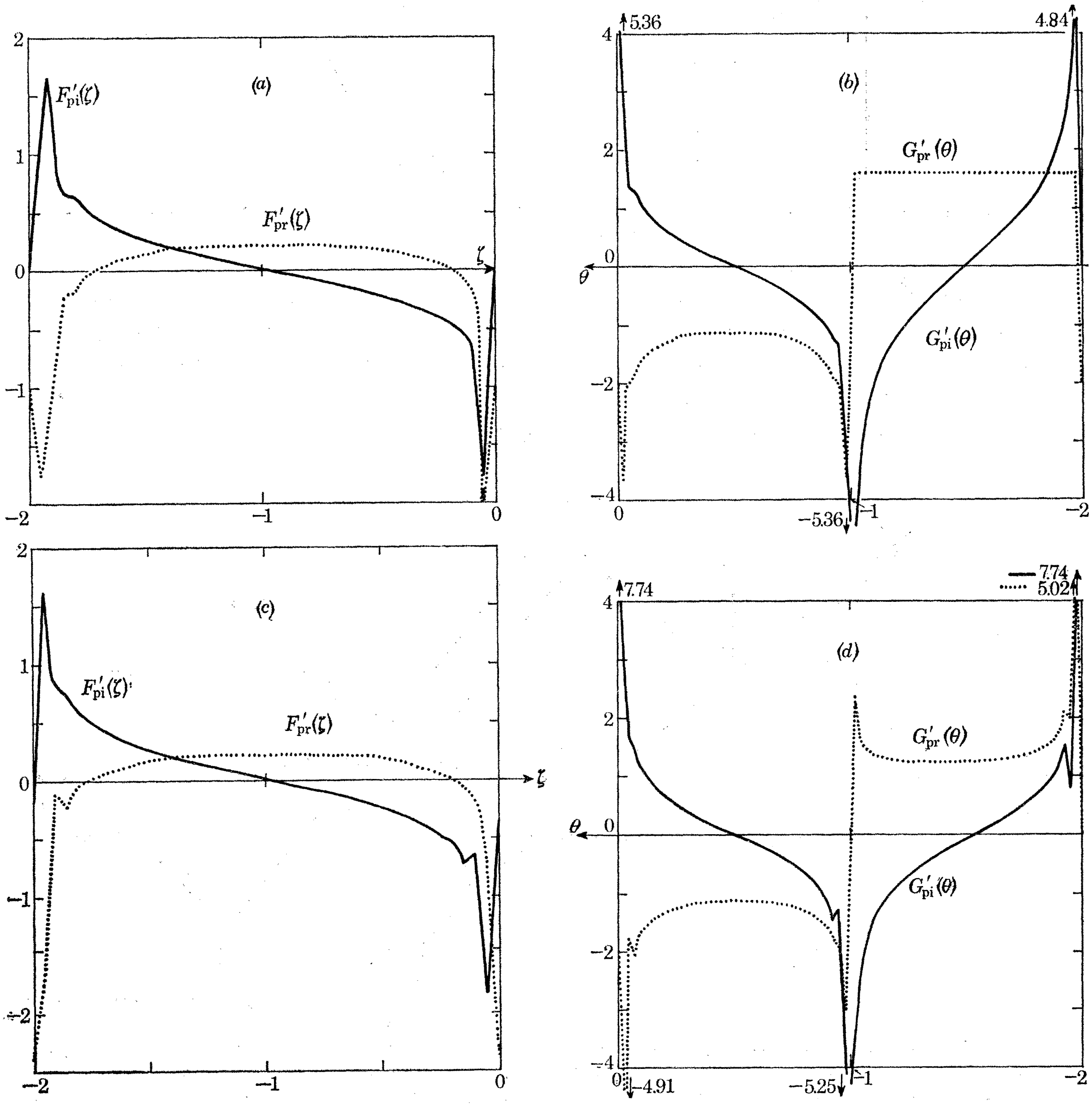

(a) l.h.s. $h_{\mathrm{L}}/h_{\mathrm{R}} = 0.5$ $s = 10000.0$

(b) r.h.s. $h_{\mathrm{L}}/h_{\mathrm{R}} = 0.5$ $s = 10000.0$

(c) l.h.s. $h_{\mathrm{L}}/h_{\mathrm{R}} = 0.5$ $s = 0.105$

(d) r.h.s. $h_{\mathrm{L}}/h_{\mathrm{R}} = 0.5$ $s = 0.105$

Figure 5 *a–d*. For description see opposite.

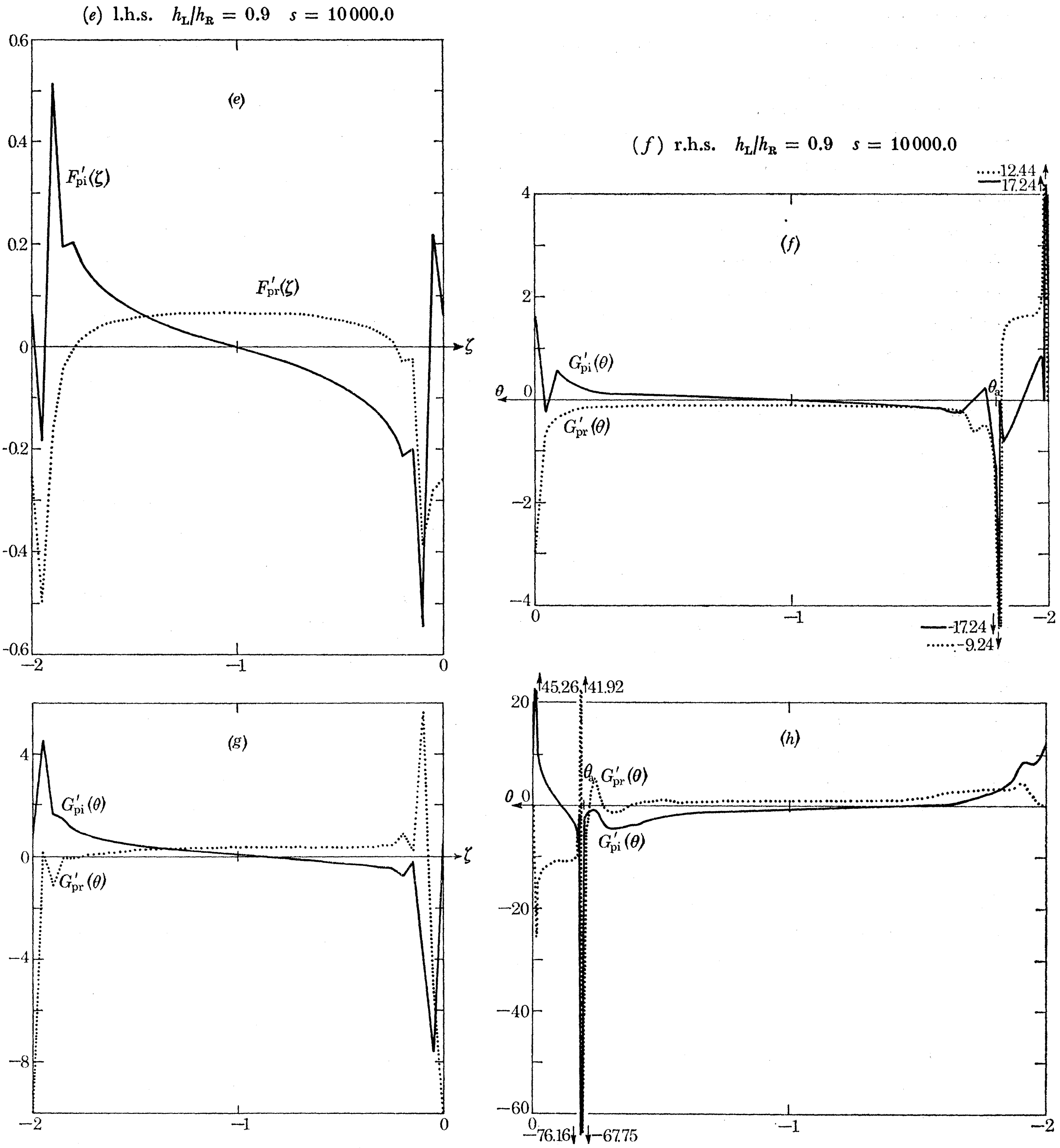

(*e*) l.h.s. $h_L/h_R = 0.9$ $s = 10000.0$

(*f*) r.h.s. $h_L/h_R = 0.9$ $s = 10000.0$

(*g*) l.h.s. $h_L/h_R = 0.1$ $s = 0.2$

(*h*) r.h.s. $h_L/h_R = 0.1$ $s = 0.2$

FIGURE 5*e*–*h*. The functions $F'_{pr}(\zeta)$, $F'_{pi}(\zeta)$, $G'_{pr}(\theta)$, $G'_{pi}(\theta)$ representing the baroclinic velocity profiles for a variety of steep linear slopes with $c = 0.1$. The velocity field in terms of these functions is given by equations (3.36), (2.35).

where $s$ is the slope of the slope. The topography is shown in figure 4. For this geometry with constant $c$ the topographic function $N(\theta)$ depends only on the ratios $h_L/h_R$, $s/c$ (as in the situation for the corresponding case in Baines (1973) where $s/c < 1$), so that the form of the solution is also only a function of these ratios.

We first consider $h_L/h_R = 0.5$, $s/c = 10^5$ (effectively infinite slope unless $c$ very large), as a representative case. This solution has many features which are common to those for all values of $s/c > 1$, $h_L/h_R$, and the variation of the wave motion with these parameters will be discussed subsequently. The main features of interest are the velocity profiles, the energy flux and its distribution and the energy density and its distribution. Velocity profiles $F'_p(\zeta)$, $G'_p(\theta)$ of the internal wave motion as functions of the characteristic variables $\zeta$, $\theta$ are shown in figures 5*a*, *b*, the relation of these ranges to the topography being shown in figure 4. The salient features of the (deep water) r.h.s. velocity profiles are (i) a nearly square-wave profile oscillating in phase with the barotropic tidal motion, and lagging 90° in phase behind it, its Hilbert transform which, in comparison, has a saw-tooth shape; (ii) two very prominent peaky regions of velocity centred around the two characteristics emanating from the top corner. The square wave in the region

$$-2.0 < \theta < -1.0,$$

when added to the initial barotropic motion $\boldsymbol{u}_1$, results in zero net in-phase† motion in the triangular corner region below the $\zeta = 0$ characteristic (and therefore, at all corresponding corners and subsequent reflecting points for these characteristics). On the (shallow) l.h.s. the velocities are comparatively smaller, the only significant feature being a 'peaky' region which is again centred on the characteristic which is tangent to the top corner. These velocity profiles are similar to those obtained by Prinsenberg (1971) for step-like topography using a procedure based on normal modes, the main differences being (apart from obvious differences due to the change in depth) that in Prinsenberg's solutions the peak velocities are smaller, and small amplitude short wavelength oscillations are present all along the profiles. Both these differences may (presumably) be attributed to truncation to a finite number of modes. The r.h.s. velocity profiles of figure 5*b* are also similar to those of Rattray *et al.* (1969) although their l.h.s. boundary conditions are different.

The energy flux and energy density (per unit surface area) for $s/c = 10^5$, $h_L/h_R = 0.5$ associated with the overall internal wave motion are both greater on the r.h.s. than on the l.h.s. by the factors 21.0 and 6.0 respectively. Consideration of the integrals for the energy and energy flux (equations (2.36), (2.37)) show that on the l.h.s. the peaky region, taken to consist of the five grid points centred on the corner characteristic ($\frac{1}{8}$ of the range), contains 76 % of the l.h.s. energy density (per unit surface area) and 50.5 % of the l.h.s. energy flux, the remainder of the energy flux being spread fairly evenly over the range with a flat secondary maximum at the characteristic furthest from the peaky region. Returning to the r.h.s. the two peaky regions (each taken as 5 grid points, $\frac{1}{16}$ of the total range, and denoted 'A' for the upper and 'B' for the lower) each contains 23.5 % of the total energy, with a sum of 47 % for the two. Minima in energy occur midway between the peaky regions. However, the energy flux is a minimum at each of the peaky regions and has two broad maxima midway between them, the energy flux from the lower region (centred on the characteristic from the bottom corner) being larger than that from the upper by a factor of approximately 2.2.

---

† 'In-phase' denotes motion in phase with the barotropic motion across the slope, while 'out-of-phase' refers to motion 90° out of phase with it.

Before proceeding further it is appropriate to note some limitations of the numerical procedure. For inviscid flow, a plane internal wave incident on a curved corner generates infinite velocities on the characteristic tangent to the corner (Baines 1971). (A concave corner presents no such difficulty, see appendix 1). In the present case the region of fluid over the slope may be regarded as the source region for internal waves, and since some of these will impinge on the slope a similar singularity will be expected. This singularity dominates the motion over a distance which is of the order of the radius of curvature of the corner, which for the present situation is a distance which is (at most) the distance between two-neighbouring grid points. It is significant that the solution is not very satisfactory in satisfying the two radiation conditions in these peaky regions, and this should be borne in mind when viewing the results below. With this sharp-cornered topography the situation is the same regardless of the number of grid-points (for comparison, topography with rounded corners is considered in the next section). Another limitation of the present numerical technique is on the closeness with which $s/c$ may approach unity; the lower corner point must lie at least one grid point away from the end of the range, which requires $s/c \gtrsim 1.025$. This may be improved by taking more grid points.

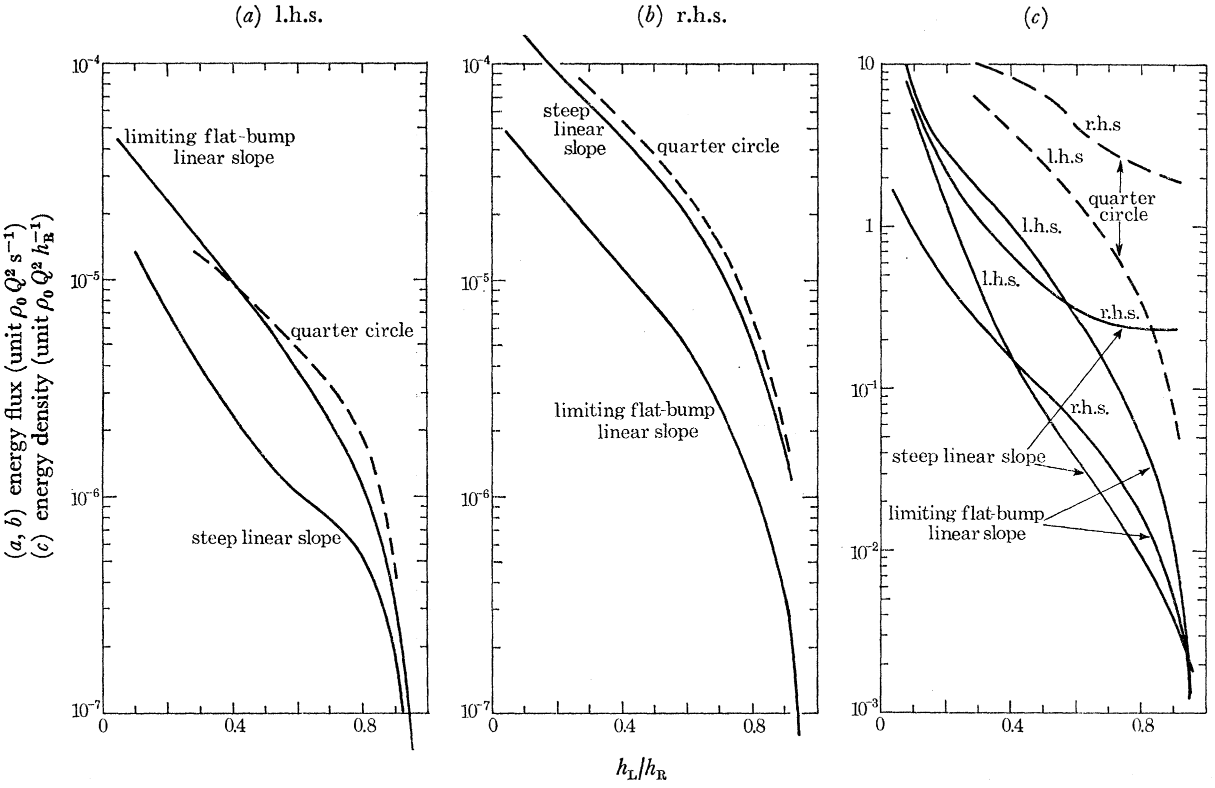
(a) l.h.s. (b) r.h.s. (c)

FIGURE 6. Energy fluxes ($a$, $b$) in units of $\rho_0 Q^2/\mathrm{s}$, and energy densities ($c$) in units $\rho_0 Q^2/h_R$ as a function of $h_L/h_R$ for the vertical linear slope ($s/c \to \infty$), the steepest flat-bump linear slope ($s/c \to 1-$), and the quarter circle slope. These figures have been drawn for $c = 1.0$ for all cases, so that these three slopes may be compared.

Velocity profiles on both the l.h.s. and r.h.s. for values of $h_L/h_R = 0.9$, 0.5 and 0.1 and for values of $s/c$ representing very steep slopes and slopes which are just steeper than the characteristic are shown in figures 5$a$–$h$. From these it may be seen that the above general description of the profiles for $h_L/h_R = 0.5$, $s/c = 10^5$ applies to every case, apart from the expected changes in proportion with $h_L/h_R$. Changes with $s/c$ appear only as comparatively minor details. From the functions $F'_{pr}(\zeta)$, $F'_{pi}(\zeta)$, $G'_{pr}(\theta)$, $G'_{pi}(\theta)$ graphed in figure 5 the horizontal and vertical velocities $u_3$ and $w_3$ may be obtained via equations (3.36), (2.35). Velocity magnitudes for other values of $c$ (but the same $s/c$) may be obtained by multiplying by the appropriate ratio of amplitude factors $A_L$, $A_R$.

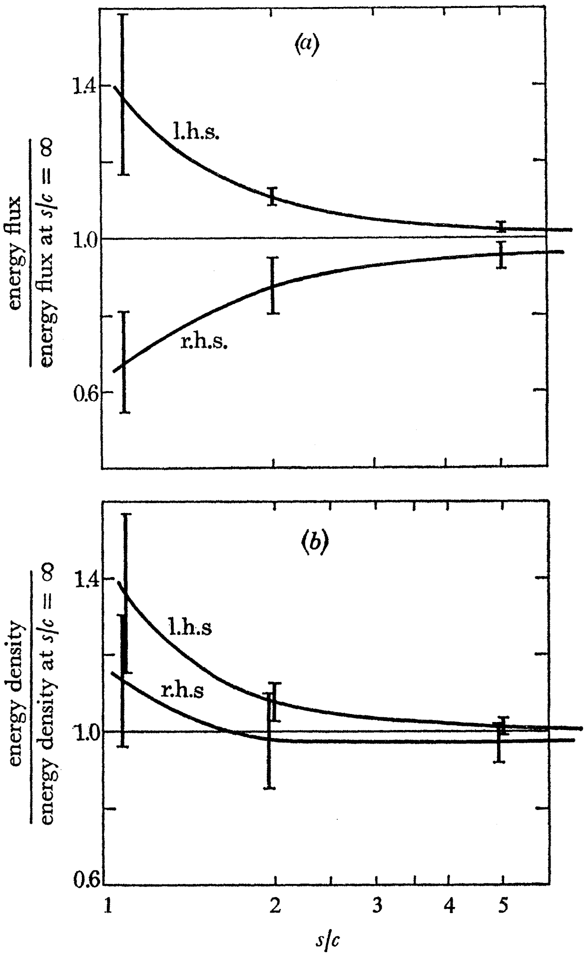

FIGURE 7. Energy fluxes (*a*) and energy densities (*b*) for linear steep slopes as a function of slope. Some scatter (particularly for $s/c$ near 1) but no systematic dependence on depth ratio $h_L/h_R$ was obtained, and the 'error bars' denote standard deviations. These curves, together with those of figure 6, contain the energy fluxes and densities for all linear steep slopes with constant stratification.

These velocity profiles show a marked similarity to corresponding profiles for $s/c$ near to but less than unity (see, for example, Baines 1973), although the velocity amplitudes are comparatively smaller on the shallow side and larger on the deeper side.† Computed velocities for the narrow 'peaky' region on the l.h.s. are larger than the corresponding barotropic velocity $Q/h_L$, though much smaller elsewhere. On the r.h.s. the in-phase baroclinic velocities are approximately half the barotropic velocity $Q/h_R$, thus resulting in zero total in-phase motion in the corner regions for steep slopes as noted above. Velocities in the r.h.s. peaky regions may be larger than the barotropic velocity.

Values for the energy fluxes and densities on both sides for steep slopes ($s/c = 10^5$) as functions

† To convert the curves of figure 8 of Baines (1973) to functions $F'_{pr}(\zeta)$ etc. on the same scale as those of figure 5 here, the scales should be multiplied by $-2.0$ for figures 8*a*, *c*, and 0.5 for figures 8*b*, *d*.

of $h_L/h_R$ are shown in figures 6*a*, *b*, *c*. The corresponding curves for flat-bump linear slopes in the limit $s/c \to 1-$ are also shown for comparison. These curves have all been drawn for $c = 1.0$ in order to compare them with those for the quarter-circle profiles, but they may readily be converted to other values of $c$ by the formulae given below. As for the flat-bump case, the energy fluxes and densities vary dramatically with $h_L/h_R$. However the dependence of these quantities on slope is comparatively slight unless $s/c$ is very close to unity, as is shown in figures 7*a*, *b*. From the numerical results no systematic variation with $h_L/h_R$ in the dependence of energy flux and density on $s$ could be detected and the curves in figure 7 represent averages of values for different $h_L/h_R$, with the 'error bars' denoting standard deviations. These fluctuations are regarded as manifestation of a limitation on the accuracy of the numerical procedure as $s/c$ approaches unity. In this limit significant contributions to both energy fluxes and densities come from the peaky regions (see below) where the solutions may be inaccurate, for reasons given above.

Energy fluxes and densities for other values of $c$ may be obtained from equations (2.36), (2.37) and figures 6 and 7, yielding, for both the l.h.s. and r.h.s.,

$$\text{energy flux }(s, c, h_L\, h_R) = \rho_0 Q^2 \frac{cN^2}{\omega}\left[\frac{E_{\text{flux}}}{cN^2/\omega}\right]_{\text{calc}}$$

$$= \rho_0 Q^2 \frac{cN^2}{\omega} \times 3.941.10^3\,(E_{\text{flux}})_{\text{calc}} \tag{5.2}$$

and

$$\text{energy density }(s, c, h_L, h_R) = \frac{\rho_0 Q^2}{h_R}\frac{1+c^2}{c(1-\omega^2/N^2)^2}\left[\frac{E_D(s/c, h_L/h_R)}{(1+c^2)/c(1-\omega^2/N^2)^2}\right]_{\text{calc}}$$

$$= \frac{\rho_0 Q^2}{h_R}\frac{1+c^2}{c(1-\omega^2/N^2)^2} \times 0.214 E_D(s/c, h_L/h_R)_{\text{calc}}, \tag{5.3}$$

where the suffix 'calc' refers to the values extracted from figures 6 and 7 for $c = 1.0$ for the desired values of $s/c$, $h_L/h_R$.

From figures 6*a*, *b* and 7*a* we see that the energy flux on the deep side is greater than that on the shallow side by a factor which depends on $h_L/h_R$ but is typically about 10 for large $s/c$; as $s/c$ decreases to 1.1 this ratio decreases by about 50 %. The *total* energy flux from simple steep slopes ($s/c \gg 1$) is approximately twice the maximum value obtainable from flat-bump slopes ($s/c \to 1-$) for virtually all values of $h_L/h_R$. As $s/c \to 1+$ this ratio decreases, but the r.h.s. energy flux for $s/c = 1.1$ is still approximately twice that for $s/c \to 1-$, so that the motion changes in a virtually discontinuous manner at $s/c = 1$.

The r.h.s./l.h.s. energy density ratio is greater than unity by two orders of magnitude for $h_L/h_R \approx 0.9$, but this decreases to nearly unity for $h_L/h_R = 0.1$. Variations of energy densities with slope (for $s/c > 1$) are comparatively slight. These results are in contrast with those for $s/c < 1$ where the energy fluxes on each side are approximately equal and the energy density is larger on the shallow side.

Finally, some remarks on the distribution of energy fluxes and densities. The l.h.s. energy flux is concentrated in the narrow region of large velocities centred on the corner characteristic, the approximate percentage of the total in this region (taken as $\frac{1}{8}$ of the characteristic range) as a function of $h_L/h_R$ being given in table 1. No dependence on slope could be detected. The r.h.s. energy flux, on the other hand, is very small in the regions of peak velocity and is mostly associated with the motion between them, the larger contribution coming from the lower range of characteristics emanating from the bottom corner region. The upper region has a flat centrally situated energy flux maximum for all $h_L/h_R$, as does the lower region except that the maximum is situated on a characteristic emanating from slightly below the bottom corner. This skews the energy flux distribution, and this $E$ flux maximum approaches the lower region of velocity maxima as $s/c \to 1+$. These characteristics of the energy flux distribution are useful as an indication of the persistence of the velocity field against attenuation processes. For example, if the wave field is advected away in a short period of time by some non-tidal motion, the region of peak velocities on the l.h.s. should reappear much more rapidly than that on the r.h.s., where the broad-scale motion should be the most prominent feature. The percentage of l.h.s. energy density in the (5 grid point) peak velocity region generally increases as $h_L/h_R$ decreases (see table 1) and has virtually no variation with slope. On the r.h.s. the energy density is concentrated in the two peak velocity regions (denoted A and B in figure 4) and the percentage of the total contained in each region varies systematically with both $h_L/h_R$ and $s/c$ (in spite of the uncertainties in velocity amplitudes previously mentioned). These variations are shown in figure 8.

TABLE 1. PERCENTAGES OF L.H.S. ENERGY FLUXES AND DENSITIES IN PEAK-VELOCITY REGION

| $h_L/h_R$ ... | 0.9 | 0.7 | 0.5 | 0.3 | 0.1 |
|---|---|---|---|---|---|
| total l.h.s. energy flux in peaky region (%) | 50 | 50 | 50 | 70 | 80 |
| energy density in peaky region (%) | 72 | 67.5 | 75 | 90.5 | 95.5 |

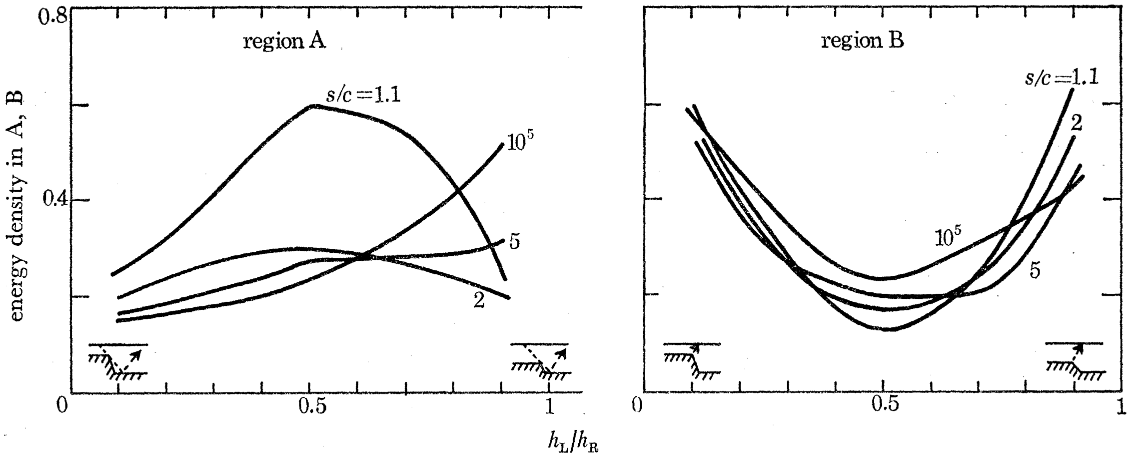

FIGURE 8. The fractions of total r.h.s. energy density, for steep linear slopes with constant stratification, contained in regions A and B of figure 4, as functions of $s/c$, $h_L/h_R$.

For a representative case with more realistic density stratification we take $c_0 = 0.01$, $c_1 = -2.16$, $h_L/h_R = 0.1$, $h_R = 1.0$ and $s = 1000$. The l.h.s. and r.h.s. energy fluxes are $2.03 \times 10^{-4} \rho_0 Q^2/s$ and $3.06 \times 10^{-3} \rho_0 Q^2/s$ respectively, and the corresponding energy densities $2.89 \rho_0 Q^2/h_R$ and $5.82 \rho_0 Q^2/h_R$, so that even with much stronger density stratification at shallow depths the motion on the deep side has greater total energy flux and density. The profiles of the functions $F'_p(\theta)$, $G'_p(\theta)$ are similar to those for $c = 0.1$ apart from the change in horizontal scale ($\theta_a = -0.52$), and larger amplitudes.

## 6. QUARTER-CIRCLE SLOPES

To complement the foregoing results for linear slopes we next consider slopes with quarter-circle profiles as shown in figure 9, and represented by the equations

$$\left.\begin{aligned} &z = -h_{\mathrm{L}}, \quad -\infty < x < x_0, \\ &z = -h_{\mathrm{R}} + [(h_{\mathrm{R}}-h_{\mathrm{L}})^2 - (x-x_0)^2]^{\frac{1}{2}}, \quad x_0 < x < x_0 + h_{\mathrm{L}}, \\ &z = -h_{\mathrm{R}}, \quad x > x_0 + h_{\mathrm{L}}, \end{aligned}\right\} \tag{6.1}$$

where $x_0 = 1/c\ (h_{\mathrm{R}} - (1+c^2)^{\frac{1}{2}}\ (h_{\mathrm{R}} - h_{\mathrm{L}}))$, is constant, the origin again being taken at the point where the tangential characteristic meets the surface. The radius of curvature is equal to $h_{\mathrm{R}} - h_{\mathrm{L}}$, and these results may be taken as representative of slopes with large radius of curvature, whilst those of the previous section relate to small radius of curvature. Typical velocity profiles are shown in figure 10 for the case $c = 1.0$, $h_{\mathrm{L}}/h_{\mathrm{R}} = 0.3$. The l.h.s. velocity profiles are very similar to those for linear slopes, indicating that the character of the l.h.s. motion is insensitive to the shape of a steep continental shelf. The r.h.s. profiles show more variation: the in-phase rectangular profile has become more triangular, the velocities in region A (as defined in § 5, see figure 10) have markedly increased and those in region B correspondingly decreased. Also, there are now velocity fluctuations which are centred around the characteristic emanating from the (smoothed) bottom corner and locally anti-symmetric about it (see appendix 1). The large velocities in region A may be attributed to the split-reflexion of internal waves at the tangent point generated over the sloping topography. Since part of the body force generating region lies below the tangential characteristic one might expect the velocity profiles to show some diffraction characteristics, i.e. Fresnel integral-like structure near region B. Oscillations of this nature are present in some cases but are not very evident in the profiles of figure 10.

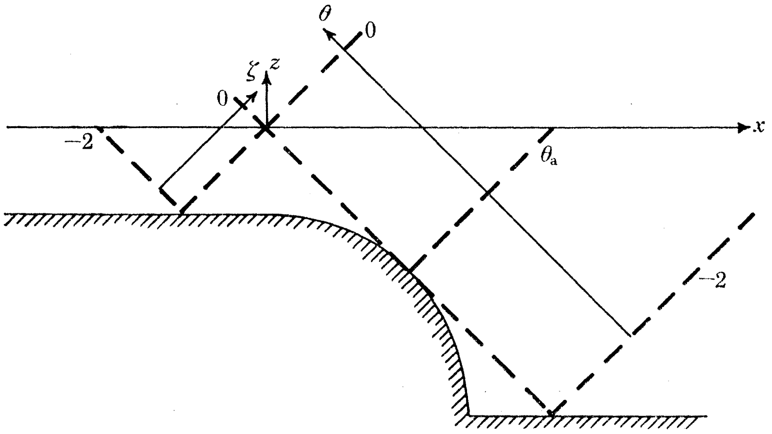

FIGURE 9. Quarter-circle slope, with $h_{\mathrm{R}}/h_{\mathrm{L}} = 0.3$, $c = 1.0$.

From figure 6 we see that in general the energy fluxes and densities are larger than for linear slopes. The larger energy densities may be essentially attributed to the large velocities in region A, while the larger energy fluxes indicate that the circular shape is a more efficient internal wave generator than the linear profile. On the l.h.s. the region of peak velocities still contains most of the energy flux, while on the r.h.s. the energy flux is very small ($< 0.5\,\%$) in region B, increases away from it on each side and has maxima near both sides of region A.

## 7. Discussion: tidal mechanisms for oceanic boundary mixing

In application to the ocean the inviscid theoretical results of the preceding sections will be modified by various turbulent and dissipative processes which may be divided into two kinds: those which are associated with the bottom boundary and boundary layer and those which are not.

The bottom boundary layer is generally turbulent (Wimbush & Munk 1971) with a critical velocity for instability (based on Ekman layers) of the order of 1 mm/s. A turbulent boundary layer on the slope implies the existence of vertical mixing, but the character and magnitude of this mixing depends very much on the nature of the turbulence in the boundary layer. Laboratory experiments with marginally unstable oscillating boundary layers reveal a spatially periodic structure which results in mixing and horizontal layering (Hart 1971; Cacchione 1970; Robinson & McEwan 1973). Whether or not the same periodic structure occurs at the higher Reynolds numbers applicable to the ocean remains to be determined. Also, experiments by Kato & Phillips (1969) on entrainment by a turbulent layer with an imposed stress yield results which may be applied to a horizontal layer but not to a sloping turbulent layer, since there is no external density gradient along the layer and the crucial phenomenon of mixed fluid leaving the layer is not present. A summary of present knowledge of entrainment processes is given by Turner (1973).

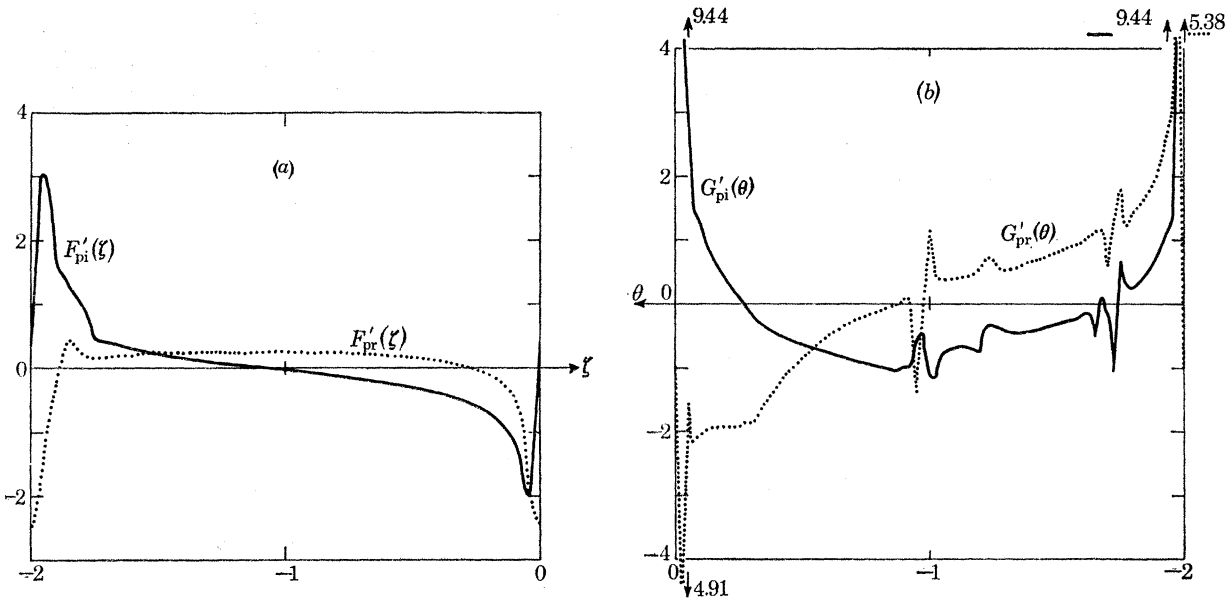
(*a*) l.h.s. $h_L/h_R = 0.3$ (*b*) r.h.s. $h_L/h_R = 0.3$

Figure 10. Velocity profile functions $F'_{pr}(\zeta)$, $F'_{pi}(\zeta)$, $G'_{pr}(\theta)$, $G'_{pi}(\theta)$ for the quarter-circle slopes with $h_L/h_R = 0.3$, $c = 1.0$, over the ranges shown in figure 9.

However, it may be assumed that the character of the turbulence will depend on the external velocity field producing it, and we compare two extreme cases, (*a*) where the external velocity is along the constant depth contours, and (*b*) where it is perpendicular to them, in the up (or down) slope direction, as in the experiments of Cacchione and Hart. We expect *a priori* that there will be greater vertical mixing in case *b* than case *a* because the turbulence may have more vigorous structure in the vertical plane and also because there will be considerable vertical displacement of the external fluid.

A second possible source of vertical mixing is that associated with the shear instability of the internal wave profile. The local Richardson number may be defined by

$$R_i = \frac{N^2}{(\partial u/\partial z)^2}, \tag{7.1}$$

where, on the l.h.s.

$$u = R_{\mathrm{e}}\left[\frac{f'_{\mathrm{p}}(\xi)}{c_0^{\frac{1}{2}}(1+c_1 z)} - c_0^{\frac{1}{2}} c_1 f_{\mathrm{p}}(\xi)\right] \mathrm{e}^{-\mathrm{i}\omega t}, \tag{7.2}$$

so that

$$R_i = N^2\Big/\left[R_{\mathrm{e}}\,\mathrm{e}^{-\mathrm{i}\omega t}\left(\frac{f''_{\mathrm{p}}(\xi)}{c^{\frac{3}{2}}} - \frac{2c_1 c_0^{\frac{1}{2}}}{c} f'_{\mathrm{p}}(\xi)\right)\right]^2 \tag{7.3}$$

$$= \frac{\omega^2 \gamma_{\mathrm{L}}^{\frac{1}{4}} c_0 (1+c_1 z)^2 (1-f^2/\omega^2+c^2)}{Q^2[(F''_{\mathrm{pr}}(\zeta) - 2c_1 c_0^{\frac{1}{2}} c^{\frac{1}{2}} \gamma_{\mathrm{L}} F'_{\mathrm{pr}}(\zeta))\cos\omega t + (F''_{\mathrm{pi}}(\zeta) - 2c_1 c_0^{\frac{1}{2}} c^{\frac{1}{2}} \gamma_{\mathrm{L}} F_{\mathrm{pi}}(\zeta))\sin\omega t]^2}, \tag{7.4}$$

where $F_{\mathrm{pr}}(\zeta)$ and $F_{\mathrm{pi}}(\zeta)$ are the real and imaginary parts of $F_{\mathrm{p}}(\zeta)$ with $Q = 1$, and similarly on the r.h.s. with $\gamma_{\mathrm{R}}$, $G_{\mathrm{p}}(\theta)$ replacing $\gamma_{\mathrm{L}}$, $F_{\mathrm{p}}(\zeta)$. When $c_1 = 0$ we have

$$R_i = \frac{\omega^2 c \gamma_{\mathrm{L}}^{\frac{1}{4}} (1-f^2/\omega^2+c^2)}{Q^2 (F''_{\mathrm{pr}}(\zeta)\cos\omega t + F''_{\mathrm{pi}}(\zeta)\sin\omega t)^2}. \tag{7.5}$$

Now it is a general property of Hilbert transforms that the maximum gradient of a function does not coincide with that of its Hilbert transform but rather with the peak value of the latter (see the velocity profiles of figures 5 and 10). Hence in order to consider the minimum values of $R_i$ as a function of $c$, $\zeta$ and $t$ it is adequate for present purposes to consider the expressions

$$\left.\begin{aligned} R_i = \frac{\omega^2 c \gamma_{\mathrm{L}}^{\frac{1}{4}}(1-f^2/\omega^2+c^2)}{Q^2 F''_{\mathrm{pr}}(\zeta)^2 \cos^2\omega t}, \quad \frac{\omega^2 c \gamma_{\mathrm{L}}^{\frac{1}{4}}(1-f^2/\omega^2+c^2)}{Q^2 F''_{\mathrm{pi}}(\zeta)^2 \sin^2\omega t}, \\ \frac{\omega^2 c \gamma_{\mathrm{R}}^{\frac{1}{4}}(1-f^2/\omega^2+c^2)}{Q^2 G''_{\mathrm{pi}}(\theta)^2 \cos^2\omega t}, \quad \frac{\omega^2 c \gamma_{\mathrm{R}}^{\frac{1}{4}}(1-f^2/\omega^2+c^2)}{Q^2 G''_{\mathrm{pi}}(\theta) \sin^2\omega t}, \end{aligned}\right\} \tag{7.6}$$

each of which relates to a particular velocity profile for given topography. We take $R_i = \frac{1}{4}$ as the criterion for onset of instability and apply these results to the velocity profiles of the previous sections, distinguishing between the stability of the 'peaks' in the r.h.s. profiles and that of the basic square-wave motion. Table 2 shows the values of $Q$ (cm²/s) necessary for $R_i < \frac{1}{4}$ for the representative cases given, with a deep water depth of 2000 m†. The most unstable profiles are those for small $h_{\mathrm{L}}/h_{\mathrm{R}}$. Equation (7.4) was used for the last case with representative oceanic stratification, where the lowest Richardson numbers occur near the surface. Invariably, the unstable part of the profile is centred on characteristics emanating from the region where a characteristic is tangent to the bottom surface.

A typical realistic value for $Q$ is $2 \times 10^5$ cm²/s (for a tidal amplitude at a coastline of 1 m and a continental shelf width of 100 km (see, for example, Baines 1973)), so that the inviscid theoretical profiles are highly unstable in oceanic conditions, particularly on the l.h.s. One may therefore hypothesize that the instability develops as a series of Kelvin Helmholtz billows along the characteristic direction which are initiated when that part of the profile becomes unstable, and result in mixing which will weaken the local density gradient and possibly result in layering. The length of this unstable region may be crudely estimated if we assume that, in each tidal cycle, the final

---

† These may conceivably be reduced by greater resolution (i.e. more grid points), so that it is more accurate to regard these numbers as *sufficient* criteria.

velocity profile obtained is smoothed by the mixing so as to be marginally stable; the instability must then be due to smaller scale components which are regenerated each cycle. The magnitude of the group velocity for waves of length $L$ is

$$|C_g| = \frac{cN^2}{(1+c^2)\,\omega}\frac{L}{2\pi} = \frac{\omega}{c}\frac{L}{2\pi}\left(1-\frac{f^2}{\omega^2(1+c^2)}\right). \tag{7.7}$$

The distance travelled by these waves in $\frac{1}{4}$-period then is

$$\frac{L}{4c}\left(1-\frac{f^2}{\omega^2(1+c^2)}\right),$$

which is a measure of the length of the unstable region from the tangent point if $L$ is taken to be its width.

Table 2

| | $h_L/h_R$ | r.h.s. (peaks) | r.h.s. (without peaks) | l.h.s. |
|---|---|---|---|---|
| $\left.\begin{matrix} c = 0.1 \\ s = 10^4 \end{matrix}\right\}$ | 0.9 | $1.9\times 10^5$ | $1.7\times 10^6$ | $1.8\times 10^7$ |
| $s = 10^4$ | 0.5 | $2.3\times 10^6$ | $2.3\times 10^6$ | $2.6\times 10^6$ |
| $s = 10^4$ | 0.1 | $1.5\times 10^4$ | $1.48\times 10^6$ | $1.5\times 10^4$ |
| quarter circle | 0.3 | $1.3\times 10^6$ | | $5.4\times 10^5$ |
| $\left.\begin{matrix} c_0 = 0.01 \\ c_1 = -2.16 \end{matrix}\right\}$ | 0.1 | | | |
| $s = 10^3$ | | $3.1\times 10^4$ | $5.3\times 10^5$ | $3.0\times 10^3$ |

The intensity of the above mixing processes, and therefore the extent to which they can affect the local density stratification, is partly controlled by the range of depths over which the topographic slope and (semi-diurnal) ray slope are nearly equal. Such near equality seems to be a common occurrence in the ocean, and this suggests that the local density stratification may be coupled to the internal tides, controlling their structure by a feed-back process.

## 8. A PRACTICAL EXAMPLE: THE ATLANTIC NEW ENGLAND CONTINENTAL SLOPE

The theory described above has been applied to a continental slope profile situated at 40° N, 70° 56′ W (approximately) for which internal wave and bottom boundary-layer measurements have been made by Wunsch & Hendry (1972) in the spring of 1970. The bottom profile is shown in figure 11 and is the same as in figure 4 of their paper except that the slope in the region of 600 m depth has been taken to be slightly less than that of the characteristic rather than greater, so that the only tangential region is that in the vicinity of 1000 m. This has been done for reasons of computational simplicity, and is justifiable in view of the general uncertainty in the precise values of $s/c$. The topography is assumed to 'level out' at depths of 130 and 2600 m, and requires a 'double-hop' formulation (figure 2*a*). The stratification used was constant below 400 m, taking a mean of the values observed by Wunsch & Hendry, and above 400 m (approximately) was based on $N^2$ profiles observed at nearby site D by Webster (1969). Two situations were taken representing summer and winter conditions respectively. A mixed layer depth of 10 m was also assumed, the bottom of which acts as a rigid reflecting surface for present purposes. The extent to which this may be justified is discussed in appendix 2. Hence the stratification is specified by (with $h_R = 2590$ m)

$$c = c_0(1+c_1 z)^2,$$

where

$$\begin{array}{llll} c_0 = 0.064, & c_1 = 0, & \text{for} & |z| > 366\,\text{m}, \\ c_0 = 0.0037, & c_1 = -\dfrac{22.35}{2590}, & & 366 > |z| > 40, \\ c_0 = 0.0037, & c_1 = -\dfrac{22.35}{2590}, & & 40 > |z| > 0, \end{array}$$

where the last range applies for summer conditions only. Winter conditions are indicated in figure 11.

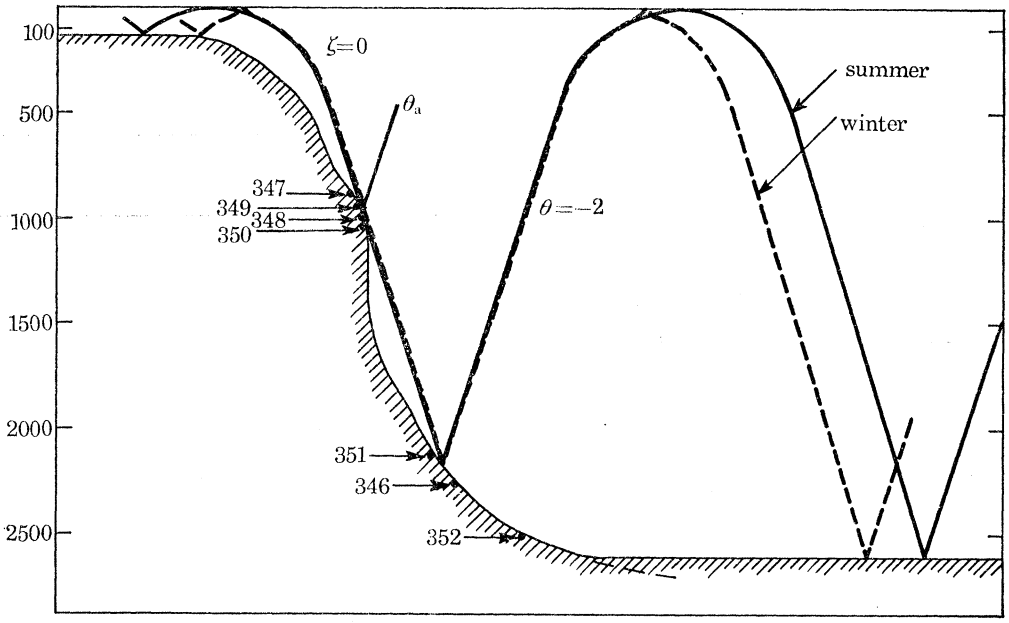

FIGURE 11. Topographic slopes and $M_2$ characteristics used in §8. Note the difference between summer and winter characteristics affected by stratification changes in the top 50 m. The numbers on the slope refer to the moorings of Wunsch & Hendry (1972).

The various topographic functions in terms of characteristic variables were constructed by graphical methods, and then smoothed over 3 grid points. (As in all the previous cases 81 grid points were used for each characteristic period on the r.h.s. and 40 on the l.h.s.) This smoothing was necessary because the velocity profiles proved to be sensitive to roughness on the scale of the grid-size owing to 'sharp-corner' effects (Robinson 1970; Hurley 1970). Genuine small-scale roughness may, in fact, be very important, but will not be considered here.

The functions $F'_p(\zeta)$, $G'_p(\theta)$ for the characteristic ranges OA and OB are shown in figure 12 for summer and winter conditions.† These may be converted into vertical or horizontal velocity profiles by means of equations (2.35), (3.1). The profiles show a much more complex structure

---

† The velocity profiles represented by $G'_p(\theta)$ are not final r.h.s. profiles, since the characteristics suffer one more reflexion from bumpy topography before entering the flat bottom r.h.s. region.

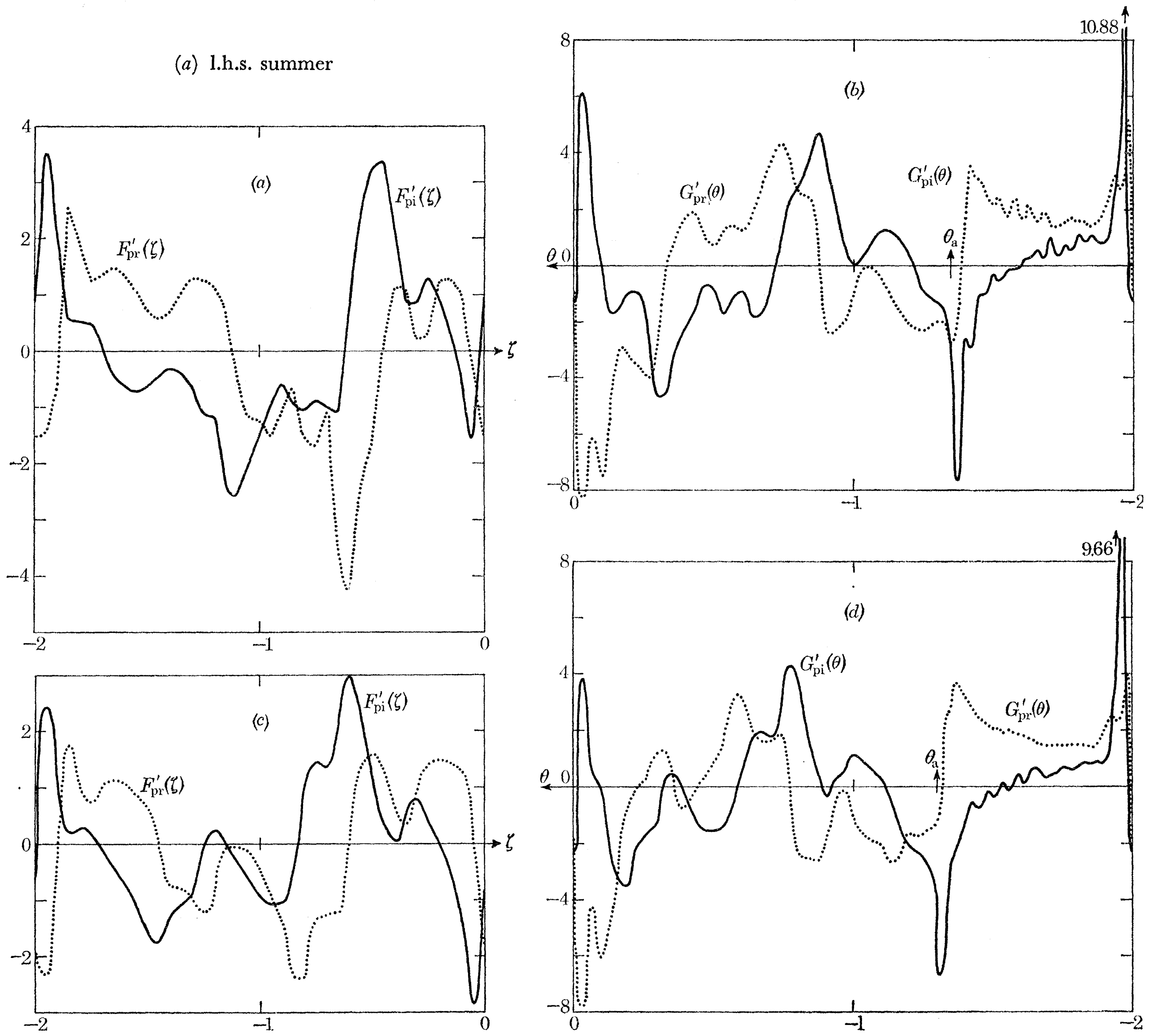

(*a*) l.h.s. summer

(*b*) r.h.s. summer, $\theta_{\mathrm{a}} = -1.353$

(*c*) l.h.s. winter

(*d*) r.h.s. winter, $\theta_{\mathrm{a}} = -1.299$

FIGURE 12. Velocity profile functions $F'_{\mathrm{pr}}(\zeta)$, $F'_{\mathrm{pi}}(\zeta)$, $G'_{\mathrm{pr}}(\theta)$, $G'_{\mathrm{pi}}(\theta)$ for summer and winter conditions for $-2 < \zeta,\ \theta < 0$ for the topography and stratification of figure 11.

TABLE 3. ENERGY FLUX, $\rho_0 Q^2 s^{-1}$ AND ENERGY DENSITY, $\rho_0 Q^2 h_{\mathrm{R}}^{-1}$

| | | |
|---|---|---|
| l.h.s., summer | $7.13 \times 10^{-5}$ | 0.807 |
| l.h.s., winter | $3.59 \times 10^{-5}$ | 0.676 |
| r.h.s., summer | $1.09 \times 10^{-4}$ | 0.651 |
| r.h.s., winter | $7.55 \times 10^{-5}$ | 0.539 |

than those for the simpler situations of the previous sections. However, the basic features of the earlier solutions, namely the square wave pattern and large velocities at its edges, are still present. The additional structure, mostly on the l.h.s. and in the range $\theta_a < \theta < 0$ on the r.h.s., may be attributed to variations in $s/c$ with depth. Since the characteristic slope 'follows' the topographic slope, small topographic bumps may easily produce regions where $s/c$ approaches unity, resulting in large wave amplitude. Differences between the summer and winter profiles are attributed principally to changes in the characteristic ranges with the stratification. The energy fluxes and densities are given in table 3. Here the figures for the l.h.s. energy density are larger than those for the r.h.s. because much of the wave motion is generated above the tangent point $P_a$, where $s/c \lesssim 1$.

Estimates of values of $Q$ required for instability of the wave field, based on the Richardson number criteria of the previous section and the gradients of the velocity profiles of figure 12 in the obvious places are given in table 4.

Table 4. Values of $Q/\mathrm{cm^2\,s^{-1}}$

| | summer | winter |
|---|---|---|
| l.h.s. | $5.0 \times 10^5$ | $3.6 \times 10^5$ |
| r.h.s. | $5.3 \times 10^5$ | $7.2 \times 10^5$ |

### *Comparison with observations*

An estimate of $Q$ may be obtained from the observations of Magaard & McKee (1973) at nearby site D (distance *ca.* 100 km). The maximum north-south velocity of their observed barotropic tidal ellipse is 0.66 cm/s. With a depth of 2600 m this yields a north-south $Q$ value of $1.72 \times 10^5\,\mathrm{cm^2/s}$. Assuming a linear decrease with distance to the nearest part of the coastline reduces this figure by a factor of $\frac{2}{3}$ at the continental slope, yielding $Q = 1.14 \times 10^5\,\mathrm{cm^2/s}$. Applying this figure to the continental slope profile in question shows that the internal wave field is everywhere stable (at least for the resolution obtained) to shear instability by the criteria of Table 4.

Horizontal velocities may now be calculated from the profiles of figure 12 by the expressions

$$u_3 = -\frac{1}{c^{\frac{1}{2}}}\frac{G'(\theta)}{\gamma_{\mathrm{M}}}Q,$$

below 366 m for the r.h.s., where $\gamma_{\mathrm{M}}$ corresponds to $\gamma_{\mathrm{R}}$ but with the depth of $P_b$ (figure 11), and

$$u_3 = -\frac{1}{c^{\frac{1}{2}}}\frac{F'(\zeta)}{\gamma_{\mathrm{L}}}Q,$$

for the l.h.s. The values for $\gamma_{\mathrm{L}}$ and $\gamma_{\mathrm{M}}$ are $5.626\,h_{\mathrm{R}}$ and $17.629\,h_{\mathrm{R}}$ respectively for summer conditions and $4.287h_{\mathrm{R}}$, $16.289h_{\mathrm{R}}$ for winter. Hence we have

$$\left.\begin{aligned} u_3 &= -0.099G'(\theta)\ \mathrm{cm/s},\\ &= -0.309F'(\theta)\ \mathrm{cm/s},\end{aligned}\right\}\ \text{summer}$$

$$\left.\begin{aligned} &= -0.107G'(\theta)\ \mathrm{cm/s},\\ &= -0.406F'(\theta)\ \mathrm{cm/s},\end{aligned}\right\}\ \text{winter}$$

for the various profiles. Since the $G'(\theta)$ values rarely exceed 4 except near the tangential characteristic the baroclinic velocities on the r.h.s. are comparable with the barotropic ones. On the r.h.s. they may be larger by a factor of 2 or 3. The total baroclinic velocity field is the sum of the velocities on the two sets of intersecting characteristics, and in the region (sufficiently far) below the tangential characteristic the baroclinic motion will partly cancel the barotropic motion, so that this region is comparatively low in energy density. Near the tangent point the baroclinic velocities are large. This region is the site of moorings 347, 348, 349 and 350 of Wunsch & Hendry (1972) (the tangent point in the theoretical model lies between moorings 348 and 349), and the highest current meters, at a distance of approximately 100 m above the bottom, correspond to a distance of about 1 grid interval above the tangential characteristic. The velocity profiles of figure 12 indicate that at this distance the baroclinic velocities will be significantly higher than those over most of the profile, and the observed r.m.s. value of 2 cm/s by Wunsch & Hendry is consistent with the present theory, as is the approximately observed ratio of $f/\omega$ for the magnitudes of the $u$ and $v$ velocities. (Larger velocities were in fact observed at 10 m, but the theory provides no basis for comparison here because of the coarse grid size.) Moorings 346, 351 at greater depths also lie in the characteristic range of large velocities around the tangential characteristic in the model, whereas mooring 352 does not, and this may explain the larger energy densities observed at the former sites. As implied above, reduced energy densities should be observed at the intermediate depths (1000–2000 m) rather than monotonically increasing energy density as suggested by Wunsch & Hendry (see fig. 10 of their paper).

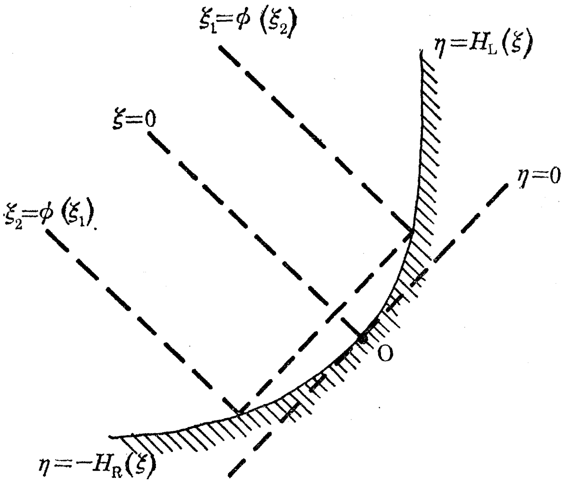

FIGURE 13. Characteristic geometry at a concave corner.

A glance at the velocity profiles of figure 12 shows that the energy is distributed among a number of modes. Using the small array of moorings 348, 349, 350, with horizontal separations of the order of 1 km, Wunsch & Hendry obtain a dominant local mode number of 2 based on the local depth, and with the measured velocities calculate an up-slope energy flux of $2.2\times10^2$ J cm$^{-1}$ s$^{-1}$.† The theoretical l.h.s. velocity profiles indicate the presence of mode 2, but it is certainly not dominant, and the extraction of a local mode number from a small group of observations is likely to be misleading in these circumstances. Effective l.h.s. mode numbers $n_e$, as defined in §2, are 1.73 (summer) and 2.9 (winter). The mean (of summer and winter) theoretical l.h.s. energy flux from table 3 and the above value of $Q$ is 0.07 J cm$^{-1}$ s$^{-1}$. This value is somewhat below

---

† C. Wunsch (private communication) has found an error in this calculation and has obtained a revised value of 0.4 J cm$^{-1}$ s$^{-1}$ for this energy flux.

the above corrected value of Wunsch & Hendry, but the discrepancy is at least partly attributable to their use of velocities near the bottom which are too high to be representative over all depths. The total (l.h.s. and r.h.s.) mean theoretical energy flux is 0.19 J cm$^{-1}$ s$^{-1}$, which indicates that this area of continental slope is unlikely to make a significant contribution to the global tidal energy dissipation.

It should be noted that the continental slope profile opposite site $D$ differs significantly from the one treated here (see Regal & Wunsch 1973, Fig. 4). In particular, there is a definite tangent point at 230 m depth, and the characteristic and topographic slopes are similar between 200 and 2000 m. Under these conditions the generated wave field is very sensitive to changes in $s$ and $c$ (witness the example of this section), and these must be known accurately to calculate the theoretical wave field with any confidence. If the internal tide at site D is predominantly generated at this continental slope, fluctuations in the stratification at the slope could account for the observed intermittency (see, for example, Magaard & McKee 1973), because of the changing spatial structure of the generated wave field. The observation that east–west baroclinic velocities are sometimes greater than north–south ones may be due to the presence of other topography as suggested by Regal & Wunsch, but an alternative plausible explanation lies in the rotation of the internal wave fronts from the east–west continental slope by horizontal shear in longer period motions.

## Appendix 1. Reflexion from a concave corner

We consider geometry as shown in figure 3 and using the same notation as in Baines (1971) we consider an incoming plane wave

$$\psi = \epsilon\,\mathrm{e}^{\mathrm{i}(k\xi-\omega t)}, \tag{A 1}$$

and a single back-reflected wave

$$\psi = \epsilon F_2(\xi)\,\mathrm{e}^{-\mathrm{i}\omega t}, \tag{A 2}$$

since no other characteristic direction extends to infinity in the fluid. $F_2(\xi)$ must satisfy

$$F_2(\xi) = \frac{\mathrm{i}}{\pi} P \int_{-\infty}^{\infty} \frac{F_2(\xi')\,\mathrm{d}\xi'}{\xi'-\xi}. \tag{A 3}$$

The reflecting surface is defined by

$$\left.\begin{aligned} \eta &= -H_{\mathrm{R}}(\xi), \quad \xi = -K_{\mathrm{R}}(\eta) \quad (\xi > 0),\\ \eta &= -H_{\mathrm{L}}(\xi), \quad \xi = -K_{\mathrm{L}}(\eta) \quad (\xi < 0),\end{aligned}\right\} \tag{A 4}$$

where all four functions are smooth, monotonic and single-valued. Near the origin, where $R$ is the local radius of curvature, we have, for $|\xi/R| < 1$,

$$H(\xi) = -\frac{(1+c^2)^{\frac{3}{2}}}{8c^2R}\,\xi^2(1+O(\xi/R)),$$

$$K(\eta) = -\operatorname{sgn}\xi\,\frac{2^{\frac{3}{2}}\,cR^{\frac{1}{2}}}{(1+c^2)^{\frac{3}{4}}}\,|\eta|^{\frac{1}{2}}\,(1+O(\eta/R)^{\frac{1}{2}}). \tag{A 5}$$

Defining the function $\phi(\xi)$ by

$$\xi > 0: H_{\mathrm{L}}(\phi(\xi)) = H_{\mathrm{R}}(\xi),$$

$$\xi < 0: H_{\mathrm{R}}(\phi(\xi)) = H_{\mathrm{L}}(\xi), \tag{A 6}$$

we have

(i) $\phi(0) = 0, \quad \phi'(0) = -1,$
(ii) $\phi(\phi(\xi)) = \xi,$
(iii) $\phi'(\xi) < 0,$ for all $\xi$,
(iv) $\phi(\xi) = -\xi,$ if the reflecting surface is symmetric in $\xi$.

If the $\eta$-motion is written $\epsilon F_1(\eta)\,\mathrm{e}^{-\mathrm{i}\omega t}$ the boundary condition $\psi = 0$ on the surface gives

$$\mathrm{e}^{\mathrm{i}k_1\xi} + F_2(\xi) + F_1(\eta) = 0, \tag{A 7}$$

when (A 4) is satisfied. As shown by figure 13 this implies

$$\mathrm{e}^{\mathrm{i}k_1\xi} + F_2(\xi) = \mathrm{e}^{\mathrm{i}k_1\phi(\xi)} + F_2(\phi(\xi)). \tag{A 8}$$

From equation (A 3) applied to both $F_2(\xi)$, $F_2(\phi(\xi))$ and (A 8) we may deduce

$$F_2(\xi) = G(\xi) + \frac{1}{2\pi\mathrm{i}}\int_{-\infty}^{\infty} F_2(\xi)'\,\frac{\mathrm{d}}{\mathrm{d}\xi'}\ln\left[\frac{\phi(\xi')-\phi(\xi)}{\xi'-\xi}\right]\mathrm{d}\xi', \tag{A 9}$$

where
$$G(\xi) = -\tfrac{1}{2}(\mathrm{e}^{\mathrm{i}k_1\xi} - \mathrm{e}^{\mathrm{i}k_1\phi(\xi)}) - \frac{\mathrm{i}}{2\pi}P\int_{-\infty}^{\infty}\frac{(\mathrm{e}^{\mathrm{i}k_1\xi'} - \mathrm{e}^{\mathrm{i}k_1\phi(\xi')})}{\phi(\xi')-\phi(\xi)}\,\phi'(\xi')\,\mathrm{d}\xi'. \tag{A 10}$$

In the case of topography symmetric in characteristic coordinates, $\phi(\xi) = -\xi$ and

$$\begin{aligned} F_2(\xi) &= G(\xi) \\ &= \mathrm{e}^{-\mathrm{i}k_1\xi}, \end{aligned} \tag{A 11}$$

regardless otherwise of the shape of the reflecting surface. From equation (A 5) we see that any smooth surface must be locally symmetric at the tangent point. This implies that, for $|\xi/R| < 1$, $F_2(\xi) = \mathrm{e}^{-\mathrm{i}k_1\xi}$ + small contributions from the integrals due to deviation from symmetry where $|\xi|$ large,

$$\begin{aligned} F_1(\eta) &= 2\cos k_1 K(\eta) + \dots \\ &= 2\left(1 - \frac{4c^2R}{(1+c^2)^{\frac{3}{2}}}\eta(1 + O(\eta/R)^{\frac{1}{2}}) + \dots\right) + \dots. \end{aligned} \tag{A 12}$$

Hence
$$F_1'(\eta) \sim \frac{-8c^2R}{(1+c^2)^{\frac{3}{2}}}, \quad F_2'(\xi) \sim -2k_1^2\xi, \tag{A 13}$$

as the corner is approached, so that the tangential velocity tends to a constant $\propto R$. The total normal velocity is

$$\frac{\mathrm{d}}{\mathrm{d}\xi}(2\cos k_1\xi) + \dots = -2k_1\sin k_1\xi + \dots,$$

so that, to leading order, the velocity locally has a stationary-wave structure, vanishing on the central characteristic and linearly anti-symmetric about it. Hence there are no singularities in the motion unless $R$ is very large.

## APPENDIX 2. REFLEXION OF INTERNAL WAVES FROM A YIELDING INTERFACE

We consider a plane internal wave represented by a stream function $\psi_\mathrm{I}$ incident from below on an interface at $z = 0$ above which lies a homogeneous layer of depth $d$ and density $\rho_0 - \Delta\rho$. The incident, transmitted and reflected waves may then be written, in the usual notation

$$\left.\begin{aligned} \psi_\mathrm{I} &= A\,\mathrm{e}^{-\mathrm{i}(k_1\eta+\omega t)}, \\ \psi_\mathrm{T} &= B\sinh k_1(z-d)\,\mathrm{e}^{\mathrm{i}(k_1 x-\omega t)}, \\ \psi_\mathrm{R} &= C\,\mathrm{e}^{\mathrm{i}(k_1\xi-\omega t)}, \end{aligned}\right\} \tag{B 1}$$

where $B$ and $C$ are complex constants and the free surface at $z = d$ is regarded as rigid. From the boundary conditions of continuity of vertical velocity and pressure at the interface (see, for example, Yih (1965) we obtain

$$A + C = -B\sinh k_1 d,$$

$$B\left[\omega\left(1-\frac{f^2}{\omega^2}\right)\left(\left(1-\frac{\Delta\rho}{\rho_0}\right)\cosh k_1 d - \frac{\mathrm{i}}{c_0}\sinh k_1 d\right) + \frac{\Delta\rho g k_1}{\rho_0\,\omega}\sinh k_1 d\right] = -2\omega\left(1-\frac{f^2}{\omega^2}\right)\mathrm{i}A/c_0, \tag{B 2}$$

where $c_0$ is the value of $c$ immediately below the interface. If $(\Delta\rho/\rho_0) \ll 1$ the last equation may be written

$$B = -\frac{2A}{\sinh k_1 d}(1-\gamma), \tag{B 3}$$

where

$$\gamma = \mathrm{i}\,c_0\left(\coth k_1 d + \frac{\Delta\rho g k_1}{\rho_0(\omega^2 - f^2)}\right),$$

so that

$$C = \frac{1-\gamma}{1+\gamma}A. \tag{B 4}$$

The density change at the bottom of a mixed layer may be regarded as a discontinuity if the distance over which the density changes is somewhat less than a vertical wavelength. With $c_0 = 0.01$ this will be the case for waves with horizontal length greater than the order of 100 m, and with $\Delta\rho/\rho_0 \approx 2.10^{-4}$, $k_1 = 2\pi/L$, we have $|\gamma| \approx 6.7$ for $L \approx 40$ km, $|\gamma| \approx 62$ for $L = 200$ m. Hence the surface layer can produce some phase change effects on the reflecting wave, but for present purposes we may take $C = -A$ as a reasonable approximation, so that the bottom of the mixed layer is regarded as rigid.

## REFERENCES

Baines, P. G. 1971 The reflexion of internal/inertial waves from bumpy surfaces. 2. Split reflexion and diffraction and diffraction. *J. Fluid Mech.* **49**, 113.

Baines, P. G. 1973 The generation of internal tides by flat-bump topography. *Deep-Sea Res.* **20**, 179.

Bell, T. H. 1973 Internal wave generation by deep ocean flows over abyssal topography. Ph.D. Thesis, Johns Hopkins University.

Cacchione, D. 1970 Experimental study of internal waves on a slope. Ph.D. Thesis, Massachusetts Institute of Technology and Woods Hole Oceanographic Institution.

Cox, C. S. & Sandstrom, H. 1962 Coupling of internal and surface waves in water of variable depth. *J. Oceanogr. Soc. Japan*, 20th ann. vol., p. 499.

Defant, A. 1961 *Physical oceanography*, vol. 2. London: Pergamon Press.

Fofonoff, N. P. & Webster F. 1971 Current measurements in the western Atlantic. *Phil. Trans. R. Soc. Lond.* A **270**, 423.

Gould, J. & McKee, W. 1973 Observations of the vertical structure of semi-diuranl tidal currents in the Bay of Biscay. *Nature, Lond.* **244**, 88.

Hart, J. E. 1971 A possible mechanism for boundary layer mixing and layer formation in a stratified fluid. *J. Phys. Oceanog.* **1**, 258.

Hurley, D. G. 1970 Internal waves in a wedge-shaped region *J. Fluid Mech.* **43**, 97.

Kato, H. & Phillips, O. M. 1969 On the penetration of a turbulent layer into stratified fluid *J. Fluid Mech.* **37**, 643.

Krause, W. 1966 *Interne Wellen.* Berlin: Gebrüder Borntraeger.

Le Blond, P. 1966 On the damping of internal gravity waves in a continuously stratified ocean. *J. Fluid Mech.* **25**, 121.

Magaard, L. & McKee, W. 1973 Semi-diurnal tidal currents at 'site D'. *Deep-Sea Res.* **20**, 997.

Munk, W. 1966 Abyssal recipes. *Deep-Sea Res.* **13**, 707.

Prinsenberg, S. 1971 Internal wave generation from a step-like, constant slope continental shelf. Ph.D. Thesis, University of Washington.

Rattray, M., Dworski, J. & Kovala, P. 1969 Generation of long internal waves at the continental slope. *Deep-Sea Res.* Suppl. to **16**, 179.

Regal, R. & Wunsch, C. 1973 $M_2$ tidal currents in the western North Atlantic. *Deep-Sea Res.* **20**, 493.

Robinson, R. M. 1970 The effects of a corner on a propagating internal gravity wave. *J. Fluid Mech.* **42**, 257.

Robinson, R. M. & McEwan, A. D. 1973 Instability of a periodic boundary layer in a stratified fluid. Submitted to *J. Fluid Mech.*

Turner, J. S. 1973 *Buoyancy effects in fluids.* Cambridge University Press.

Webster, F. 1969 Vertical profiles of horizontal ocean currents. *Deep-Sea Res.* **16**, 85.

Wimbush, M. & Munk, W. 1971 The benthic boundary layer. In *The sea*, vol. IV, (ed. A. E. Maxwell), p. 731. New York: Pergamon.

Wunsch, C. & Hendry, R. 1972 Array measurements of the bottom boundary layer and the internal wave field on the continental slope. *Geophys. Fl. Dyn.* **4**, 101.

Yih, C. S. 1965 *Dynamics of non-homogeneous fluids.* New York: Macmillan.